Vilnius University

Faculty of Physics

Laser Research Center

Kawthar Reggui

SURFACE FUNCTIONALIZATION OF TRANSPARENT MATERIALS BY DIRECT LASER INTERFERENCE PATTERNING

Final Thesis

Europhotonics master program

Student	Kawthar Reggui
Defense date	2023-08-29
Supervisor	Dr. Laura Loi
Consultant	Prof. Audrius Dubietis
Reviewer	Dr. Domas Paipulas
Laser Research Center Director	Dr. Dalia Kaškelytė

Vilnius 2023

Contents

1 Introduction

Surface functionalization at the micro- and nano-scale enables local modification of material properties, tailoring them to obtain new and outstanding characteristics, such as superhydrophobicity [1], friction control, and anti-reflection [2]. These new properties open the door for these materials to be used in different applications in emerging markets, such as biomedical devices, micro-optics, biotechnology, and microfluidics. Such effects can be observed in nature. A well-known example is the lotus effect [3], where the superhydrophobic or self-cleaning property of the lotus leaf results from the well-defined micro- and nanostructures on the surface of the leaves.

Conventionally, surface functionalization has been accomplished through lithographic methods with wet chemical etching or reactive ion etching [4]. Nevertheless, this approach is a multi-step process that employs hazardous chemicals [5], posing potential adverse impacts on both human health and the environment. Laser-based texturing methods present an attractive alternative to lithography-based techniques in producing accurate surface patterns in the micrometer and nanometer scale. Furthermore, they can provide high processing speeds with little to no preparation or post-processing [6]. Among laser-based texturing methods, Direct Laser Interference Patterning (DLIP) appears as a more versatile approach for the fabrication of deterministic microstructures [7]. DLIP is a technique based on overlapping multiple laser beams to induce an interference pattern onto the material surface. By controlling the number of interfering beams and their overlapping angle, the wavelength of the radiation, and the deposited fluence, it is possible to achieve different patterns, periodicities, and aspect ratios [8].

Transparent materials are commonly used in many established and emerging industries, such as microelectronics, photovoltaics, optical components, and biomedical devices [8]. Therefore, the functionalization of transparent materials through the DLIP technique appears as a promising tool to tailor their optical and mechanical surface properties for applications in different fields. For instance, for anti-reflection applications in the visible range, the period of the desired structures has to reach values much smaller than the sub-micron scale ($< 300nm$). To achieve these structures, it is necessary to employ today's tailored optics and scanning systems that allow reaching these numbers. Hence, in this work, we investigate the processability of two transparent materials, sapphire, and polycarbonate, by 343nm-wavelength femtosecond laser DLIP, using a custom-made f-theta lens with a large aperture (d=20 mm) and a small focal length (F30mm).

2 Basic theory

2.1 Surface functionalization

Most surface properties found in nature, such as the lotus effect, are related to well-defined micro- and nanostructures inherent to these surfaces [9]. The lotus effect, which refers to the superhydrophobic property of the lotus leaf, is primarily attributed to the presence of micro- and nano-scale structures on the leaf's surface, as illustrated in Fig. 1. These structures create a combination of hydrophobicity and self-cleaning properties. As a result, dirt and other contaminants are less likely to adhere to the surface, making it easier for water to remove them [3].

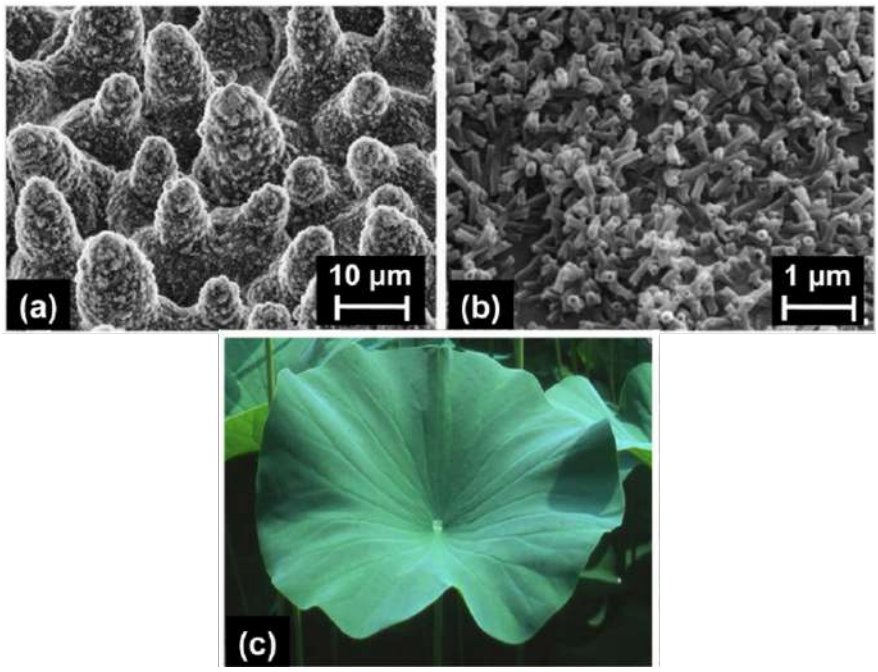

Figure 1 : SEM images of the microstructures **(a)** and nanostructures **(b)** in the Lotus leaf **(c)**. Adapted from [3].

Another example that can be found in nature is the blue iridescent colors in the wing scales of the Morpho butterflies [10]. As shown in Fig. 2, the wing contains 3D nanostructures that diffract the incident light. Multiple interferences from the stacked-layer structure are responsible for the strong blue irradiance.

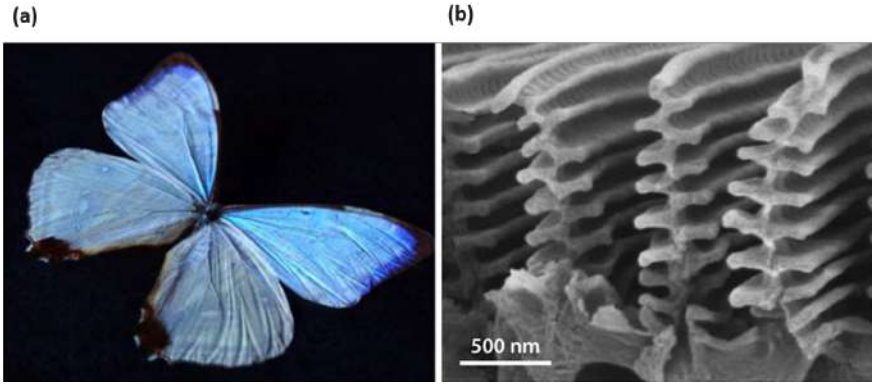

Figure 2 : **(a)** A photograph of Morpho didius butterfly showing blue iridescence **(b)** SEM image of the nanostructures on the butterfly wing. Adapted from [10].

An interesting example of anti-reflection properties in nature is the transparent wings of the Greta oto butterfly, commonly known as the glasswing butterfly. The wings exhibit exceptional low haze and reflectance across the entire visible spectral range, even at wide viewing angles of up to 80° [11]. This omnidirectional anti-reflection behavior is attributed to the presence of small nanopillars covering the transparent regions of its wings, as shown in Fig. 3.

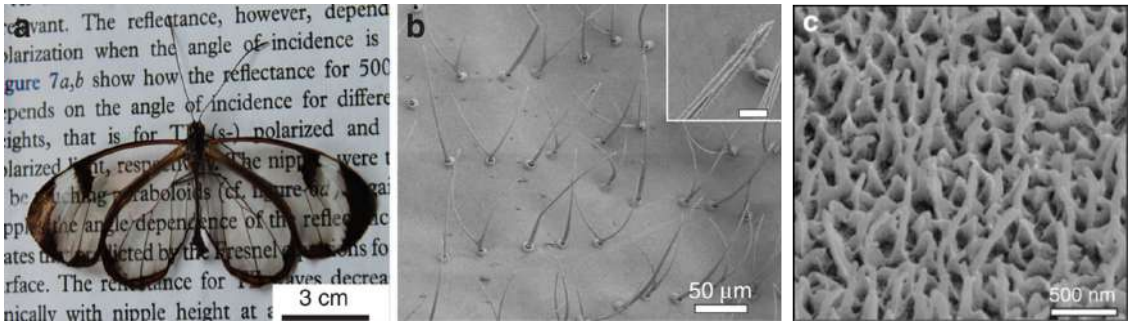

Figure 3 : **(a)** Photograph of a glasswing butterfly (Greta oto). Its wings feature three regions: transparent, dark brown, and white. **(b)** SEM image of the transparent region revealing that this part of the wing is covered with $\approx 2\ \mu m$ thick and $\approx 40\ \mu m$ long bristles or micro-hairs. The areas between these micro-hairs are covered with nanopillars **(c)**. Adapted from [11].

These natural effects have inspired the development of different methods to texture the surfaces of different materials in order to alter or improve their properties. As a result, these materials can be utilized in various applications in different industries.

Surface functionalization is usually carried out through lithographic techniques combined with wet chemical etching or reactive ion etching [4]. These techniques enable patterning structures in the micrometer and the nanometer scale with high aspect ratios and excellent uniformity. Nevertheless, they consist of multiple steps, require a prefabricated mask, and use dangerous chemicals [5].

Laser-based texturing techniques have emerged as a promising alternative for precise and con-

trolled material structuring at the micro- and nano-scales. Furthermore, they can provide high processing speeds with little to no preparation or post-processing [6]. There exist three main approaches to achieve laser surface texturing: Direct laser writing (DLW), patterning by the generation of laser-induced periodic surface structures (LIPSS), and DLIP.

In DLW, a single laser beam is guided by a scanner and focused onto the surface of the material, as illustrated in Fig. 4. A large variety of materials can be processed, depending on the laser wavelength, pulse duration, and pulse energy. For instance, this technology has been used to create superhydrophobic microstructures on aluminum as well as on titanium [12, 13]. However, this approach is limited by the processing speed as well as the available beam size, which restricts the achievable feature size [14]. In LIPSS texturing, it is possible to obtain structures in the submicrometer range [8]. Although surface texturing based on LIPSS is a relatively simple process, features with high aspect ratios are hard to achieve and their periodicity is limited by the laser wavelength used for their generation, and its polarization state [15]. A typical setup for LIPSS processing is illustrated in Fig. 4.

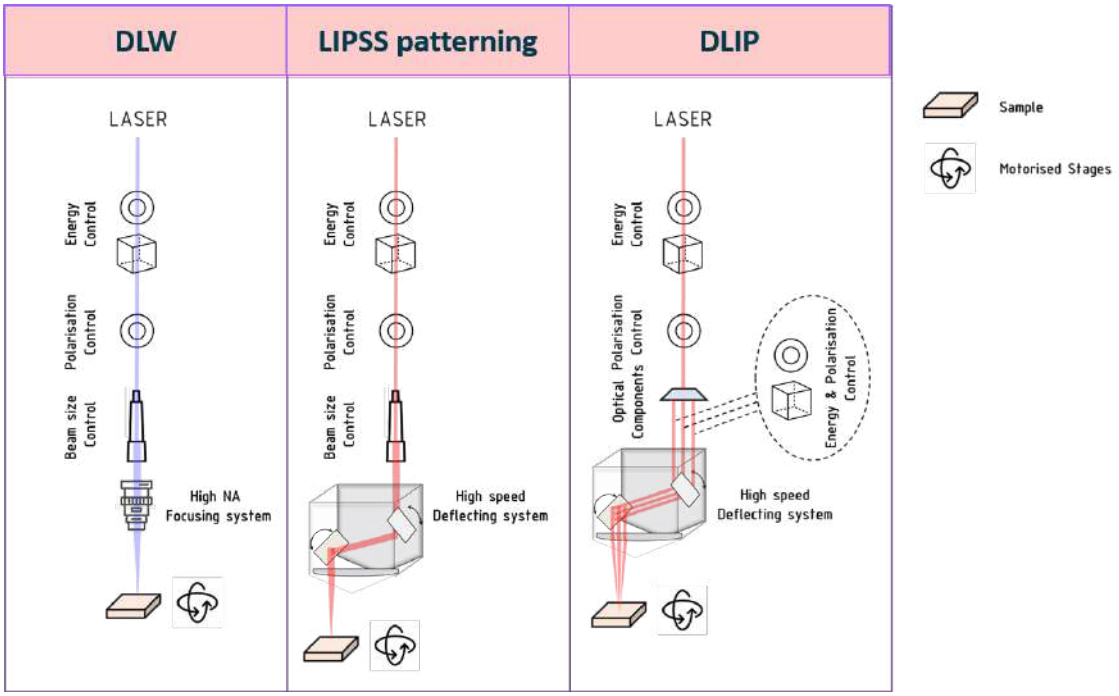

Figure 4 : Schematic of the experimental setup of DLW, LIPSS patterning, and DLIP. Adapted from [16].

Among these laser-based texturing methods, DLIP technique has attracted a growing interest as it offers a combination of throughput, flexibility, and resolution [7]. The DLIP method relies on the superposition of at least two laser beams, as shown in Fig. 4, thereby producing a periodic variation

of the laser intensity. By controlling the number of interfering beams and their overlapping angle, the wavelength of the radiation, and the deposited fluence, it is possible to obtain different pattern geometries, periodicities, and aspect ratios [8].

2.2 Direct laser interference patterning

The theory of the DLIP method can be first approached by considering the interference of two linearly polarized monochromatic plane waves. Each plane wave is defined by [17]:

$$E_i(r,t) = E_i cos(\omega t - k_i.r + \phi_i), \tag{1}$$

where E_i is the amplitude, ω is the angular frequency, k_i is the wavevector, ϕ_i is the phase, and $i = 1, 2$. The resulting electrical field upon overlapping the two beams is expressed as:

$$E(r,t) = E_1(r,t) + E_2(r,t), \tag{2}$$

the total time-independent intensity distribution $I(r)$ at the overlap of the two waves is expressed as the absolute square of the sum of the electrical fields:

$$I(r) = |E_1(r) + E_2(r)|^2, \tag{3}$$

by substituting the expressions of the electrical fields, we obtain:

$$I(r) = I_0[1 + \frac{E_1 E_2}{I_0} cos(k_0 2sin(\theta)y + \phi_1 - \phi_2)], \tag{4}$$

where $k_0 = \frac{2.\pi}{\lambda}$ and the term I_0 is expressed as $I_0 = \frac{1}{2}(E_1^2 + E_2^2)$. From the cosine term, it is evident that the interference of the two plane waves produces a one-dimensional fringe pattern with a periodicity Λ directly proportional to the wavelength λ and inversely proportional to the sine of the angle θ between each wavevector and the z-axis line, as illustrated in Fig. 5.

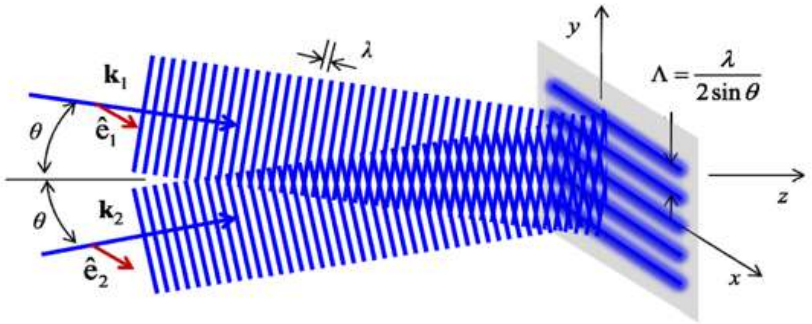

Figure 5 : Two-beams interference: Interference pattern at the x-y plane with a periodicity of Λ is formed by two linearly-polarized monochromatic plane waves. In this example, k_1 and k_2 are contained in the y-z plane at an angle θ with respect to the z-axis [17].

In the general case with N interfering beams, the form of the total intensity distribution $I_T(r)$ is expressed as [17]:

$$I_T(r) = I_0[1 + \sum_{j>i}^{N} V_{ij} cos((k_j - k_i).r + \phi_i - \phi_j)], \tag{5}$$

where I_0 is now $\frac{1}{2}\sum_1^N E_k^2$ and the coefficient V_{ij} is defined as:

$$V_{ij} = \frac{E_i E_j}{I_0}. \tag{6}$$

Every beam-pair combination produces a 1D fringe pattern, each defined by a spatial-cosine term with the magnitude V_{ij}, which contributes to the overall periodic intensity distribution. For instance, considering the interference of three beams, the three beams defined by k_1, k_2, and k_3 interfere at the x-y plane at a common angle of incidence θ with respect to the z-axis, as illustrated in Fig. 6. The beam pairs (k_1,k_2), (k_1,k_3), and (k_2,k_3) form three distinct 1D-interference fringe patterns. When two of these pairs are combined, they form a square lattice pattern, when then combined with the remaining pair, they result in a hexagonal lattice. The periodicity of the resulting pattern is directly proportional to the beam wavelength and inversely proportional to the sine of the angle of incidence θ [17].

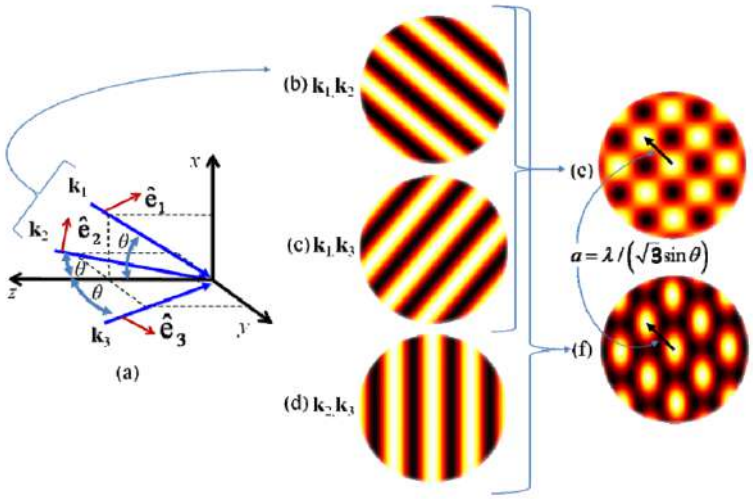

Figure 6 : Three-beam interference: **(a)** Three beams defined by k_1, k_2, and k_3 interfering at the x-y plane at an angle of incidence θ with respect to the z axis. The beam pairs defined by **(b)** k_1 and k_2, **(c)** k_1 and k_3, and **(d)** k_2 and k_3 form three different 1D-interference patterns. **(e)** The fringes patterns of (k_1,k_2) and (k_1,k_3) combine to form a square lattice **(f)** The 1D pattern of (k_2,k_3) combines with the other two fringe patterns to form a hexagonal lattice with periodicity of $\frac{\lambda}{\sqrt{3}sin(\theta)}$ [17].

Eq. 5 indicates that the shape of the obtained pattern is defined by the number of overlapping beams. Figure 7 shows examples of different configurations of interfering beams and the resulting interference patterns. In these cases, the beams are arranged symmetrically with the same overlapping angle θ and azimuthal angles ϕ, and all the beams have the same phase and polarization direction [7].

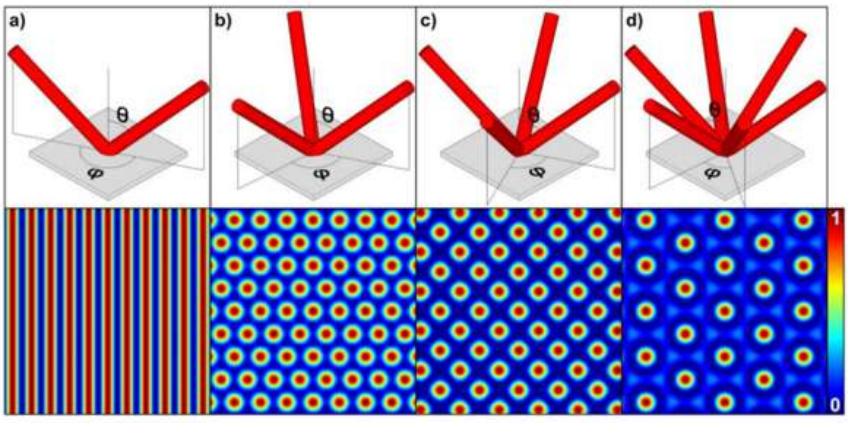

Figure 7 : Schematic showing the set-up (upper row) and the resultant patterning (lower row) with **(a)** two, **(b)** three, **(c)** four and **(d)** six overlapping beams together with the calculated intensity of each interference pattern [7].

Eq. 5 also demonstrates that the spatial period depends on the beam wavelength and the sine of the angle of incidence (i.e. overlapping angle θ). Therefore, in order to obtain structures with

small periodicity, it is necessary to work at short wavelengths (e.g. UV) as well as increase the overlapping angle, by separating the beams as much as possible and working at a short focal length.

2.3 Ultrashort pulsed laser

Ultrafast lasers are laser sources that emit light pulses shorter than a few picoseconds. This unique property, in addition to their high peak powers, enabled new opportunities for high-quality and high-precision processing of a wide range of materials, with minimal thermal damage [18], as illustrated in Fig. 8.

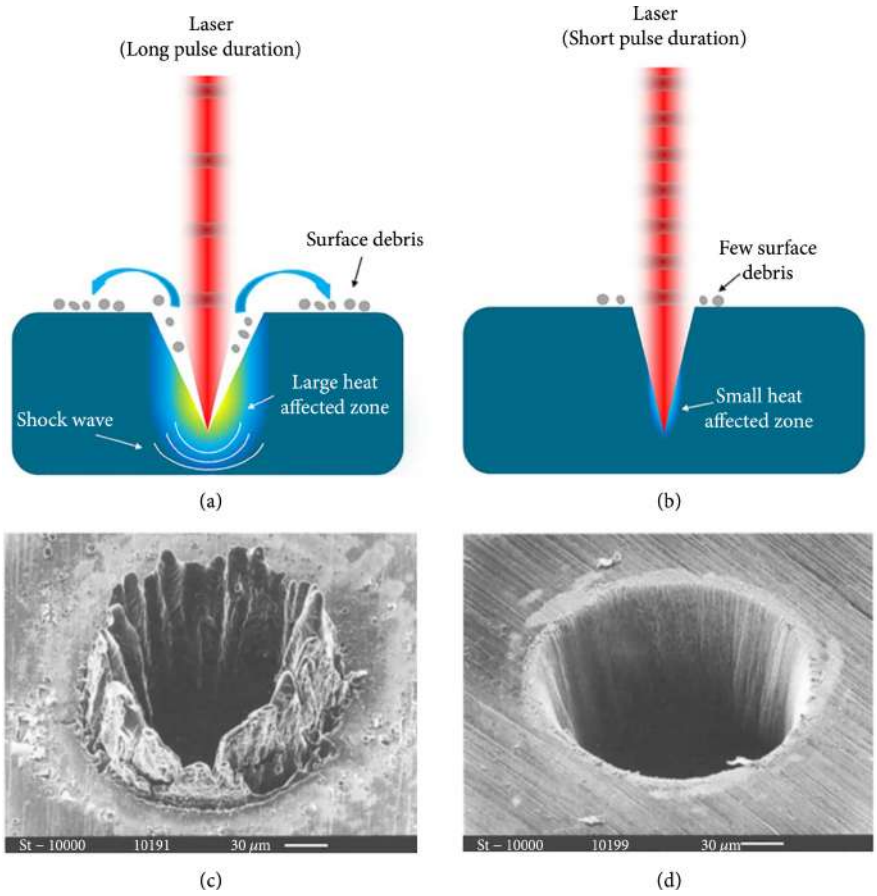

Figure 8 : Schematic of laser interaction with materials under different pulse durations: **(a)** long pulse duration and **(b)** short pulse duration. SEM images of laser ablated holes fabricated on a 100 μm steel foil by **(c)** 780 nm nanosecond laser of 3.3 ns, 0.5 J/cm^2 and **(d)** 780 nm femtosecond laser of 200 fs, 0.5 J/cm^2 [19].

As depicted in Fig. 9, the energy deposition from ultrafast lasers to the material is faster than the electron-bulk diffusion rate, which allows for non-thermal processes, leading to high-precision processing of the material, as shown in Fig. 8d. Moreover, ultrafast lasers can induce nonlinear absorption effects, such as multiphoton absorption or tunneling ionization, which allow for efficient

material processing. This makes it possible to work with transparent or difficult-to-machine materials, such as glass, plastics, and ceramics, without the need for complex post-processing steps [18].

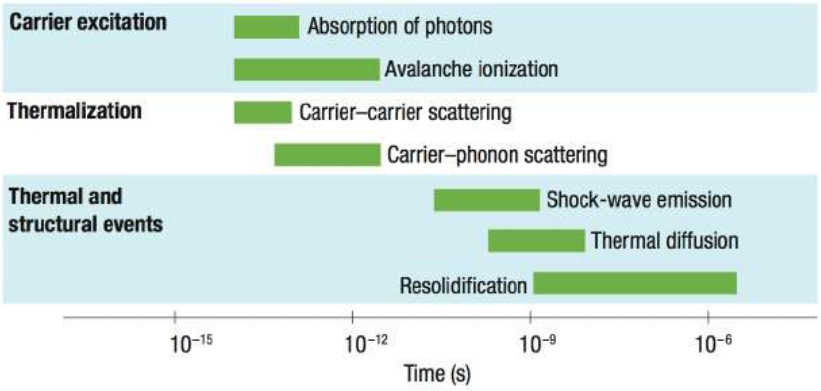

Figure 9 : Plot of the timescales involved in the femtosecond laser-material interaction. While most of the energy is absorbed in the femtosecond time range, changes in material continue to evolve well into the microsecond range [20].

2.4 Laser-matter interaction

In the case of allowed transitions, the laser interacts with the material by creating an electron-hole plasma through linear absorption. In the case of wide-bandgap materials, the processes involved are far more complex. In those materials, the energy of individual photons is insufficient to jump the large band gap and be linearly absorbed by the material. Instead, the valence electrons are transferred to the conduction band via nonlinear processes, such as multiphoton ionization, tunnel ionization, and avalanche ionization [21].

2.4.1 Multiphoton absorption

Multiphoton absorption (MPA) occurs when several photons with energy lower than the bandgap energy E_g are simultaneously absorbed by the material to excite a valence band electron, as illustrated in Fig. 10b.

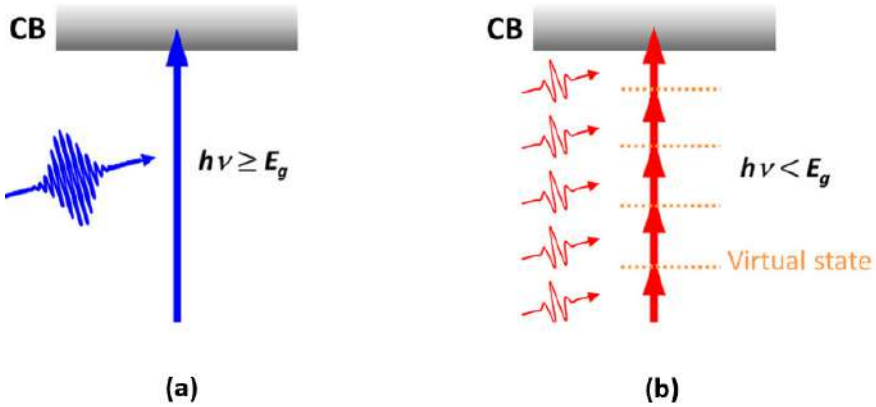

Figure 10 : Electron excitation process in materials by single **(a)** and multiphoton absorption **(b)** [22].

The MPA process is described by the following rate equation:

$$\frac{dN}{dt} = \gamma I^m \tag{7}$$

where $\frac{dN}{dt}$ is the number of photons excited per unit of time, I is the intensity of the incident light, and γ is the frequency-dependent absorption coefficient for the m^{th} order absorption. The terms with $m > 1$ are collectively referred to as nonlinear absorption [23]. The number of photons required for MPA is determined by the smallest m that satisfies the relation $mh\nu > E_g$, where E_g is the band-gap energy of the dielectric material, and $h\nu$ is the photon energy [21].

At intense laser field, the band structure and potential barrier between valence and conduction bands of the material can be distorted, allowing the valence electrons to directly tunnel to the conduction band in a time shorter than the laser period, as illustrated in Fig. 11a. This effect is known as the tunneling ionization effect.

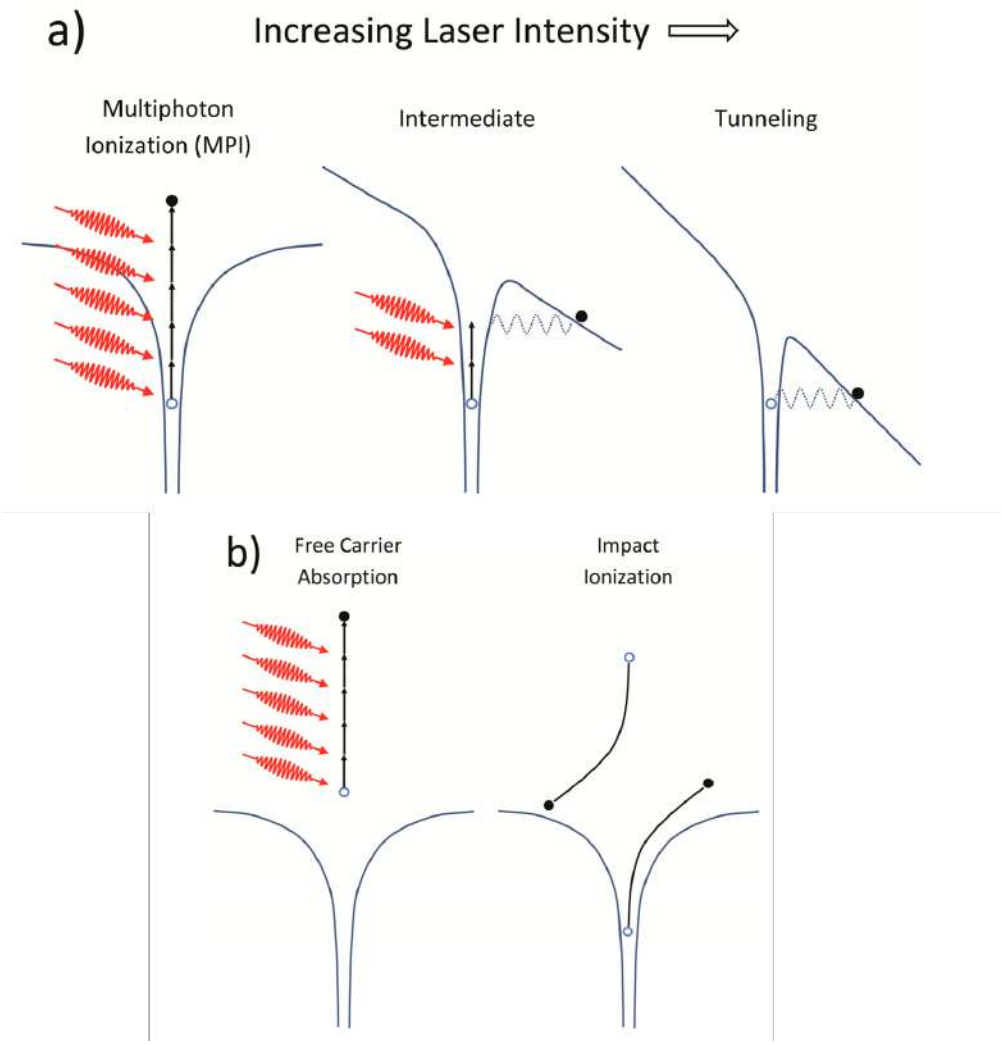

Figure 11 : Schematic of free electron plasma formation with high-intensity pulses where **(a)** multi-photon and tunneling ionization generates free electrons that **(b)** absorb radiation and impact-ionize surrounding material resulting in avalanche ionization. [24].

The transition from MPA to tunneling ionization is characterized by the Keldysh parameter [25]:

$$\gamma = \omega \frac{\sqrt{2mI_0}}{eE_0} \tag{8}$$

where m_e is the mass of the electron, I_0 is the ionization potential of the atom, e is the charge of the electron, and ω and E_0 are the frequency and the electric field amplitude of the laser source. MPA dominates when γ is much larger than 1, which is the case of most materials-related investigations of laser interactions with dielectrics [21].

2.4.2 Avalanche ionization

The avalanche ionization process involves the free-carrier absorption process, followed by impact ionization, as illustrated in Fig. 11b. The free-carrier absorption process occurs when the electrons already existing in the conduction band further absorb incident laser light. This process requires a sufficient quantity of seed electrons in the conduction band. These seed electrons can arise from thermally excited impurity or defect states or, in our case, from direct multiphoton and/or tunneling ionization. As a result, these electrons are transferred from an already-excited state to another state in the same band (intra-band absorption), where they can impact ionize bound electrons. Such process gives rise to more free electrons that also undergo the free carrier absorption process and impact ionize even more bound electrons. As long as the laser field is sufficiently high, this process keeps repeating itself, generating an electron avalanche, which leads to materials breakdown, triggering ablation and material damage [24].

3 State of the art

DLIP technique has been widely utilized to functionalize metallic and non-metallic surfaces [7]. Table 1 lists some examples of different materials processed with DLIP, and the corresponding laser parameters (wavelength and pulse duration, etc).

Stainless steel is one of the most extensively studied metals with DLIP. Madelung et al. fabricated periodic microstructures on stainless steel using a galvanometer-scanner DLIP approach. Using a nanosecond pulsed laser source operating at a wavelength of 527 nm, line-like patterns with spatial periods ranging from 2.9 to 12.8 μm were produced [14], as depicted in Fig. 12.

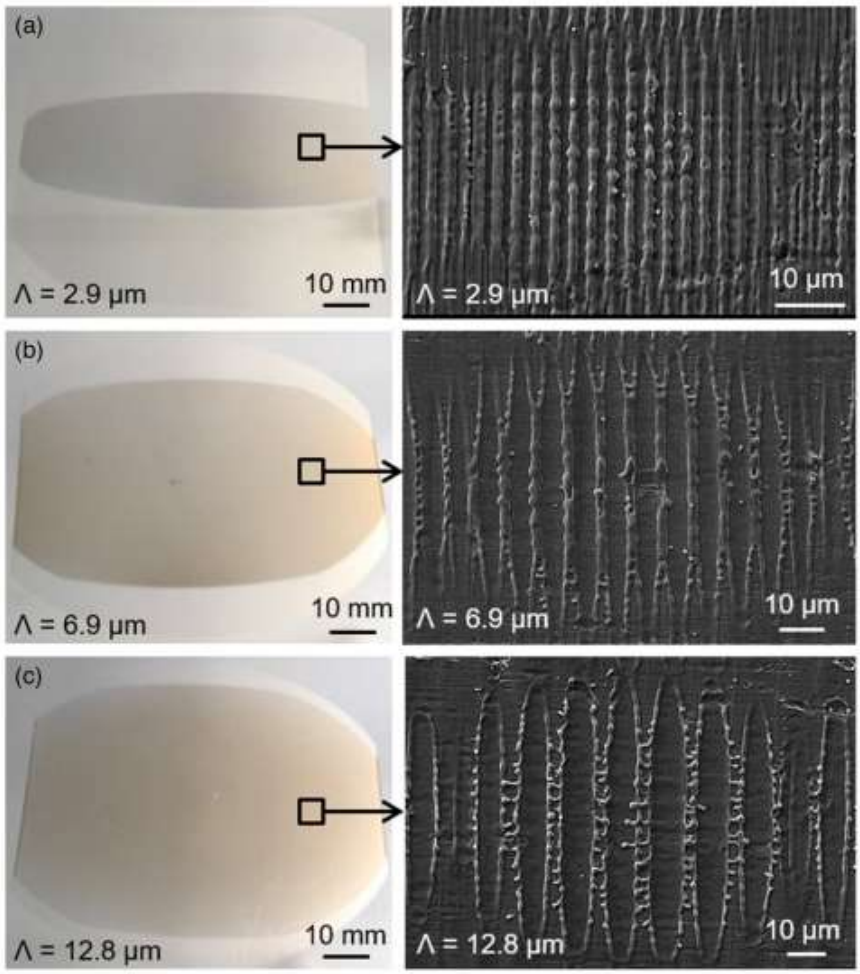

Figure 12 : Optical and SEM images of the DLIP-treated scan fields for a spatial period of **(a)** $\Lambda = 2.9\ \mu m$, **(b)** $\Lambda = 6.9\ \mu m$, and **(c)**$\Lambda = 12.8\ \mu m$ [14].

Table 1 . Examples of materials processed with DLIP, and the corresponding laser parameters (wavelength and pulse duration, etc). The number of beams used and the obtained periodicity are also indicated.

Material	Wavelength	Pulse duration	Repetition rate	Method	Number of beams	Periodicity	Ref.
Stainless steel	527 nm	5 ns	3.5 kHz	DOE and prism Scanner-based	2 beams	2.9 µm 6.9 µm 12.8 µm	[14]
Stainless steel	1030 nm	10 ps	3 kHz	Beam splitter Translation stages	2 beams	850 nm	[26]
Aluminium	1064 nm	10 ps	10 kHz	DLIP optical head (Fraunhofer IWS) High precision axes	2 beams	2.6 µm	[27]
PET	266 nm	10 ns	10 Hz	Beam splitter Translation stages	2 beams	1.8 µm 2.6 µm	[28]
Polycarbonate	263 nm	3 ns	1 kHz	DLIP optical head (Fraunhofer IWS) Translation stages	2 beams	2.6 µm	[29]
Si	532 nm	200 fs	*	DOE and prism Translation stages	4 beams 6 beams	600 nm 2 µm 5 µm	[30]
Diamond	800 nm	100 fs	10 Hz	Beam splitter Translation stages	2 beams	2.5 µm	[31]
Silica	800 nm	100 fs	10 Hz	Beam splitter Translation stages	2 beams	1 µm	[32]
Silica	800 nm	120 fs	1-1000 Hz	Beam splitter Translation stages	3 beams	1.9 µm 2.2 µm 3 µm (Vertical period)	[33]
Sapphire	800 nm	100 fs	10 Hz	Beam splitter Translation stages	2 beams	1.6 µm 2.7 µm	[34]
Soda lime	532 nm	12 ps	10 kHz	DOE and prism Translation stages	2 beams 4 beams	2.3 µm 4.7 µm	[8]

Regarding polymers, polycarbonate (PC) and polyethylene terephthalate (PET) are among the first polymeric materials to be structured by DLIP. For example, PC sheets have been structured using a two-beam interference arrangement with an ultraviolet (263 nm) nanosecond-pulsed laser [29], creating line- and pillar-like structures with simple and hierarchical geometries, with a periodicity down to 2 μm, as illustrated in Fig. 13.

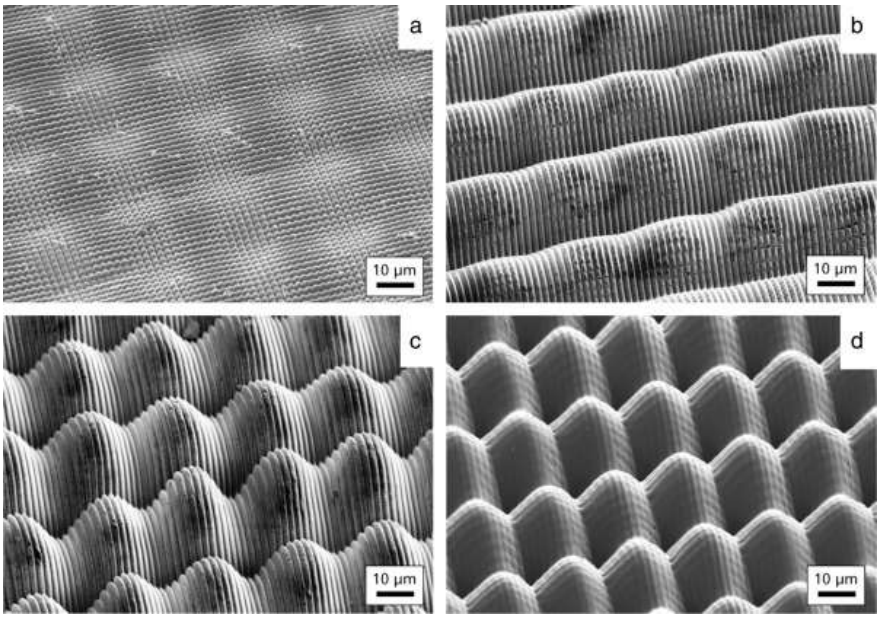

Figure 13 : SEM images of simple and hierarchical structures in PC, depicting **(a)** pillar-like structures (fluence: $0.51 J/cm^2$, overlap: 10 pulses), **(b)** lines on line-like structures perpendicularly orientated fluence ($0.51 J/cm^2$, overlap: 90 pulses), **(c)** lines on pillar-like structures (fluence: $1.63 J/cm^2$, overlap: 90 pulses) and **(d)** pillars on pillars-like structures (fluence: $1.63 J/cm^2$, pulses: 120) [29].

Concerning dielectrics, Kawamura et al. conducted groundbreaking studies focused on performing DLIP on diamond [31], silica glass [32], and sapphire [34] using femtosecond pulses in the near infrared range. In these studies, the beam was split into two beams, then crossed on the sample's surface. An optical delay line was used to adjust the two beams precisely, both spatially and temporarily to produce the interference pattern. In diamond, it was possible to achieve a periodicity of 2.5 μm. In silica, the group fabricated a 1D pattern with a periodicity down to 1 μm. On sapphire two different periodicities were achieved by changing the overlap angle. At $\theta = 17°$ the periodicity was $\gamma = 2.7\ \mu m$, and at $\theta = 30°$, the achieved periodicity was $\gamma = 1.6\ \mu m$, as illustrated in Fig. 14.

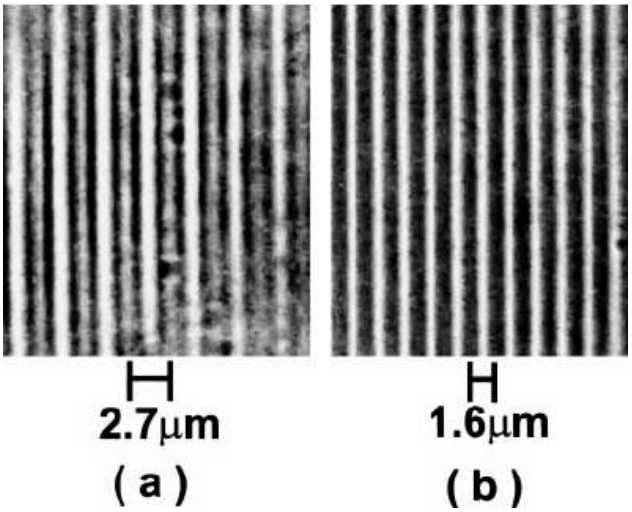

Figure 14 : Optical micrographic photos of surface relief-type gratings encoded on sapphire by holographic irradiation with fs laser pulses at $\theta = 17°$ **(a)** and $\theta = 30°$ **(b)** [34].

The surface structuring of soda lime glass using picosecond (ps) pulses in the visible radiation (532 nm) was studied by Alamri et al. by interfering two and four beams [8]. A full systematic study was performed by varying the spatial period and fluence dose and linking them with controlled surface properties, as shown in Fig. 15. Line- and dot-like patterns were fabricated with spatial periods between 2.3 and 9.0 μm and aspect ratios up to 0.29. The fabricated micropatterns act as relief diffraction gratings, which split incident light into diffraction modes.

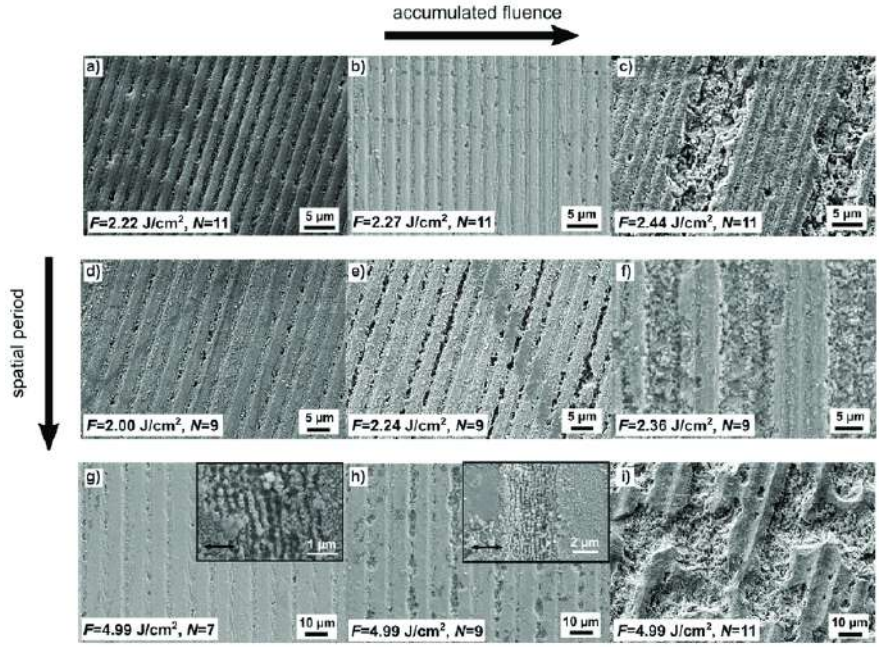

Figure 15 : SEM images of glass samples structured with line-like patterns and different spatial periods: **(a-c)** 2.3 μm, **(d-f)** 3.9 μm, and **(g-i)** 9.0 μm. The accumulated fluence dose increases from left to right [8].

4 Methodology

4.1 Two-beams DLIP experimental setup

To pattern the 1D fringes, the experiment was conducted using a two-beam setup, which is shown in Fig. 16.

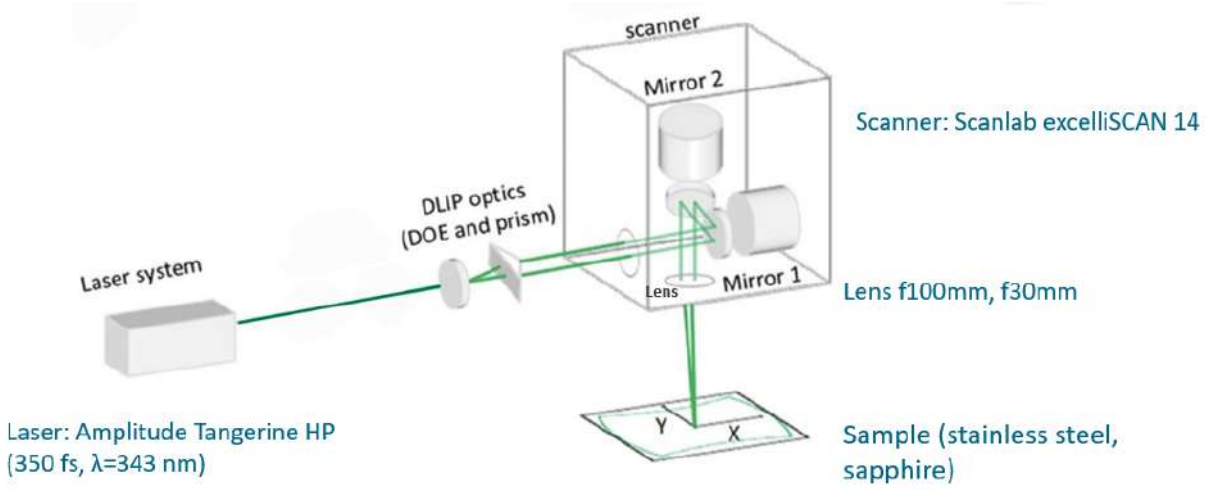

Figure 16 : Schematic setup of the two beams DLIP system. DOE: Diffractive optical element. Adapted from [14].

A femtosecond laser (Tangerine HP, Amplitude) emitting pulses with a duration of 350 fs and a wavelength of 343 nm was used. The setup also consisted of a double spot diffractive optical element (DOE) that splits the primary beam coming from the laser source into two beams. The two beams were then parallelized by a 159.42° apex angle prism. After passing through the galvanometer scanner (Scanlab excelliSCAN 14), the two beams were focused by an f-theta lens onto the surface of the sample. As a first step, a lens with a focal length of 100mm ($F100mm$) was employed in the study. The lens was then replaced with a lower focal length lens ($F30mm$) to ensure a smaller periodicity with the same setup. The spatial period of the pattern could be modified by adjusting the distance between the DOE and the prism.

In this setup, DLIP was performed on two materials: stainless steel and sapphire. Since stainless steel is easier to process, it was employed initially to verify the presence of the interference pattern and to measure the periodicity of the pattern.

4.2 Four-beams DLIP experimental setup

The four-beams setup was used to pattern the hexagonal structure onto the surface of the sample. The experimental setup was similar to the one used for the two-beams configuration. However, a 2x2 spots DOE was used instead, in addition to a pyramidal angle prism to parallelize the beams, as depicted in Fig. 17.

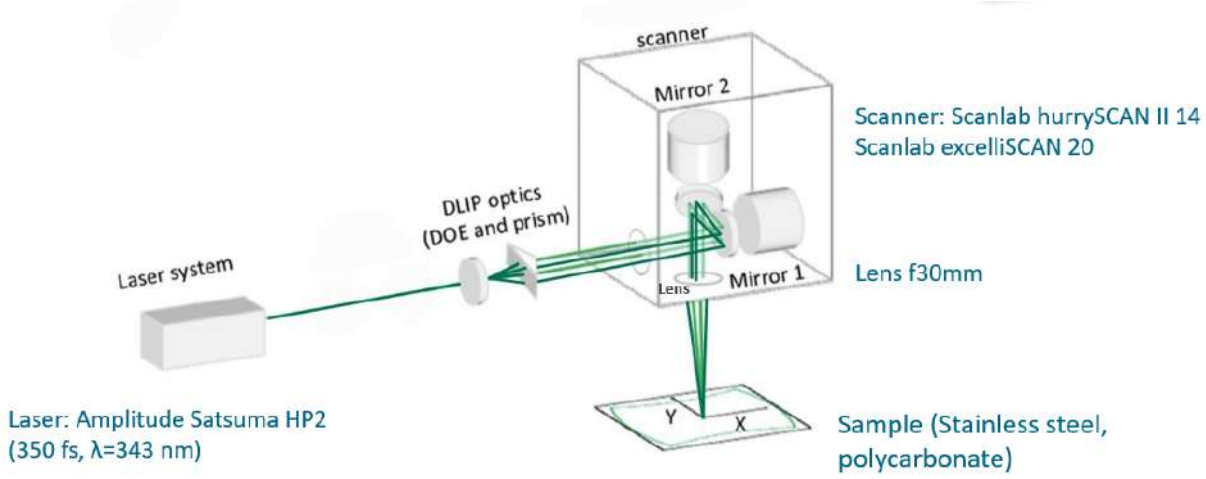

Figure 17 : Schematic setup of the four beams DLIP system. DOE: Diffractive optical element. Adapted from [14].

In this setup, the laser source was a femtosecond laser (Satsuma HP2, Amplitude) that emits pulses with a duration of 350 fs and a wavelength of 343 nm. The study was initially performed with the galvanometer scanner Scanlab hurrySCAN II 14. To ensure the maximum separation between the beams, and hence decrease the periodicity of the pattern, the scanner was replaced with a different scanner with a larger entrance (Scanlab ExcilliSCAN 20). The beams were directed by the two mirrors inside the scanners onto the f-theta lens ($F30mm$), which focused the beams onto the surface of the sample. The experiment was performed with two different samples: stainless steel and PC.

4.3 Patterning strategy

To texture large areas, the pulses can be shifted in the vertical and horizontal directions, as depicted in Fig. 18.

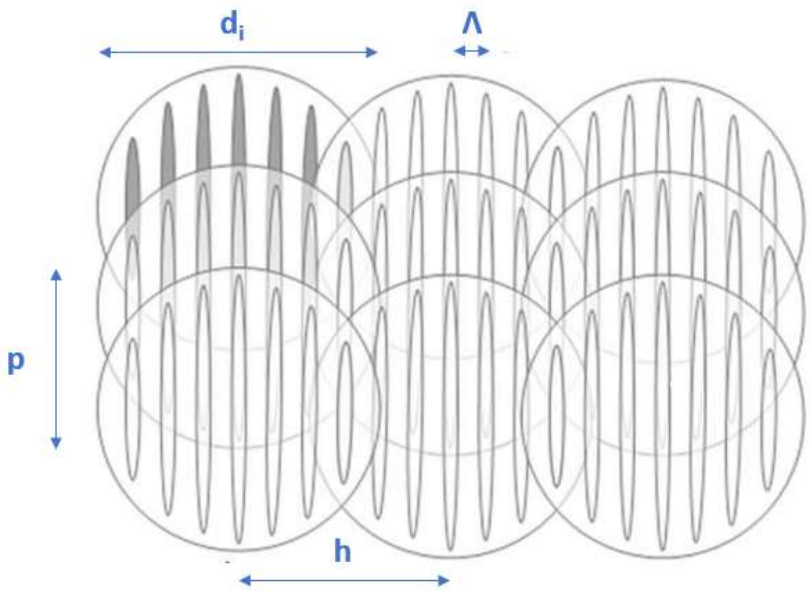

Figure 18 : Patterning strategy for producing homogeneous microstructures. d_i is the laser spot diameter, Λ is the periodicity, p is the overlap distance between the pulses, and h is the hatch. Adapted from [14].

Since the laser pulses are emitted at a certain repetition rate f, by adjusting the speed of the scanner v, the laser spots can be displaced in the vertical direction with a defined distance d, which can be calculated by:

$$d = \frac{v}{f} \tag{9}$$

As demonstrated in the formula below, the distance d can be tuned to obtain different overlaps between the successive pulses:

$$p = 1 - \frac{d}{d_i} \tag{10}$$

where p is the overlap, d is the pulse separation distance, and d_i is the spot diameter. The different overlaps indicate different amounts of accumulated fluence dose in the material. After completing a vertical line, the scanner mirrors are moved to guide the laser spots in the horizontal direction to start a new vertical line. The horizontal distance between the vertical lines is referred to as the hatch distance h. Since this displacement is perpendicular to the direction of the interference lines, the hatch distance must be selected to be an integer multiple of the spatial period so as to overlap the intensity maxima positions, and hence avoid the deterioration of the structure produced in the previous pulses. In order to obtain homogeneous DLIP-textured regions, different values of overlap and hatch were investigated at different pulse energies.

4.4 Surface characterization

The surface topography measurements were carried out through a ZEISS Smartproof 5 wide-field confocal microscope, with 50x/0.95 objective. The surface morphology of the treated samples was analyzed with a scanning electron microscope (SEM) VEGA3 by TESCAN.

5 Results and discussion

5.1 Two-beams DLIP

In a preliminary investigation conducted on stainless steel using an f-theta lens with a focal length of 100mm, the speed of the scanner was augmented to separate the pulses. For a repetition rate of 10kHz, the speed was adjusted to $v = 3m/s$. This step is essential to confirm the presence of the interference pattern and to measure its periodicity. Moreover, in order to determine the pulse separation distances corresponding to various overlaps, it is necessary to measure the diameter of the beam spot diameter as well. As illustrated in Fig. 19, following the separation of pulses, the pattern's tilt angle was found to be $\alpha = 10°$. Consequently, subsequent inscriptions were made along this angle so as to prevent the destruction of the patterns created by previous pulses. The measured spot diameter was $d_i = 70\ \mu m$. The calculated pulse separation distances and scanner speed values are detailed in Table 2.

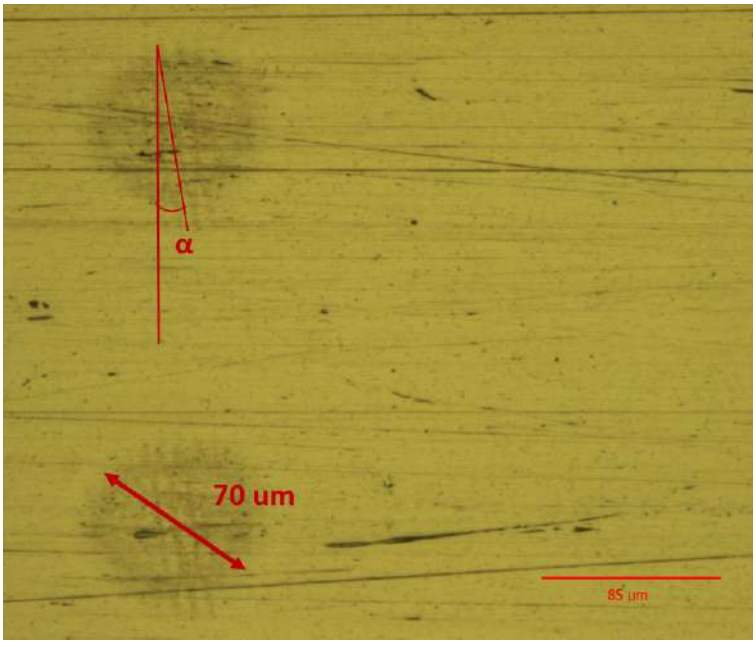

Figure 19 : Preliminary experiment on stainless steel with the $F100mm$ lens. The speed of the scanner was increased to separate the pulses: for a repetition rate of 10kHz, the speed was set as $v = 3m/s$. The measured tilt angle of the pattern was $\alpha = 10°$ and the spot diameter was $d_i = 70\ \mu m$.

Table 2 . The different pulse separation distances corresponding to different overlaps, and the corresponding scanner speed.

Overlap p in %	50	60	70	80	90
Distance between successive pulses (μm)	45	28	21	14	7
Corresponding scanner speed (m/s)	1.35	0.84	0.63	0.42	0.21

The overlaps listed in Table 2 were carried out at different pulse energies, and an optimum value of pulse energy was chosen ($E_p = 36.05\ \mu J$), where the DLIP structure was most homogeneous, and the thermal effects were minimal. From Fig. 19, the measured spatial period of the pattern was 7.3 μm. To ensure proper alignment between the consecutive pulses, the hatch distance was chosen to be an integer multiple of this spatial period. Consequently, three specific hatch values were selected for further studies, namely: $h = 15, 22, 30\ \mu m$. Using the previously identified parameters, a series of $2x2mm^2$ square structures were fabricated, varying the overlaps and hatches. This procedure was iterated with different numbers of passes, as depicted in Fig. 20.

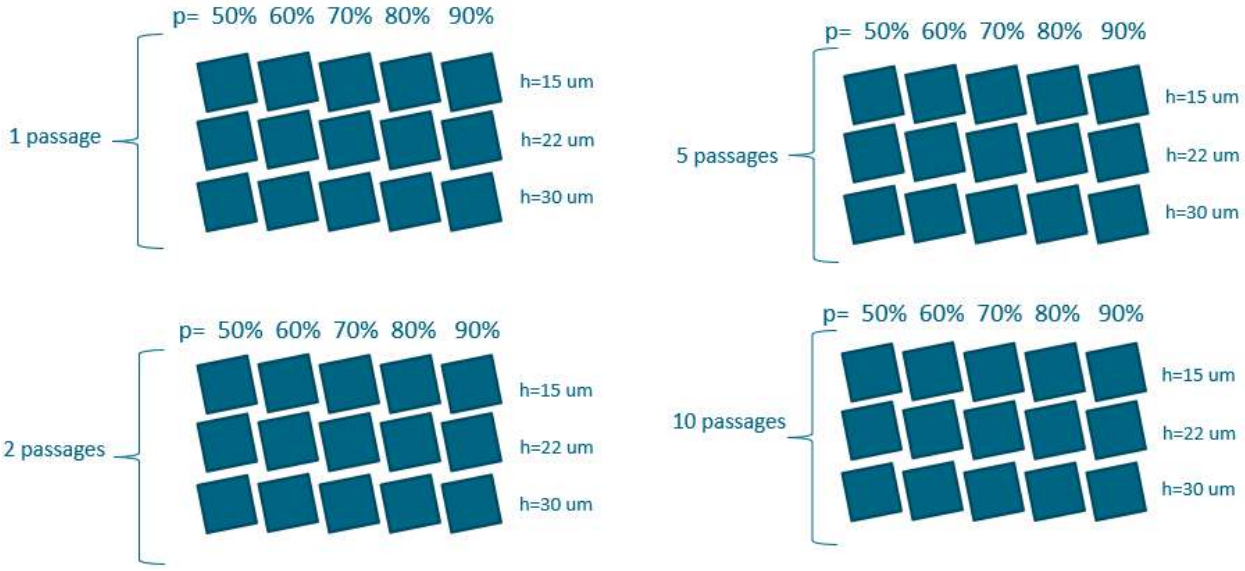

Figure 20 : $2x2mm^2$ squares were produced at $E_p = 36.05\ \mu J$, at different overlaps and hatches. Each matrix corresponds to a specific number of passages. The rows correspond to different hatch values, and the columns correspond to different overlaps.

For the case of $h = 15\ \mu m$, when the overlap was increased from 50% to 90%, the accumulated fluence increased as well, which resulted in an augmentation in the depth of the trenches from 0.05 μm to 0.3 μm as depicted in the line profiles in figures 21b and 21d, respectively. Yet, the surface non-homogeneity was still apparent. This lack of homogeneity is reflected in the fast Fourier transform (FFT) spectrum shown in Fig. 21e, where several peaks can be observed.

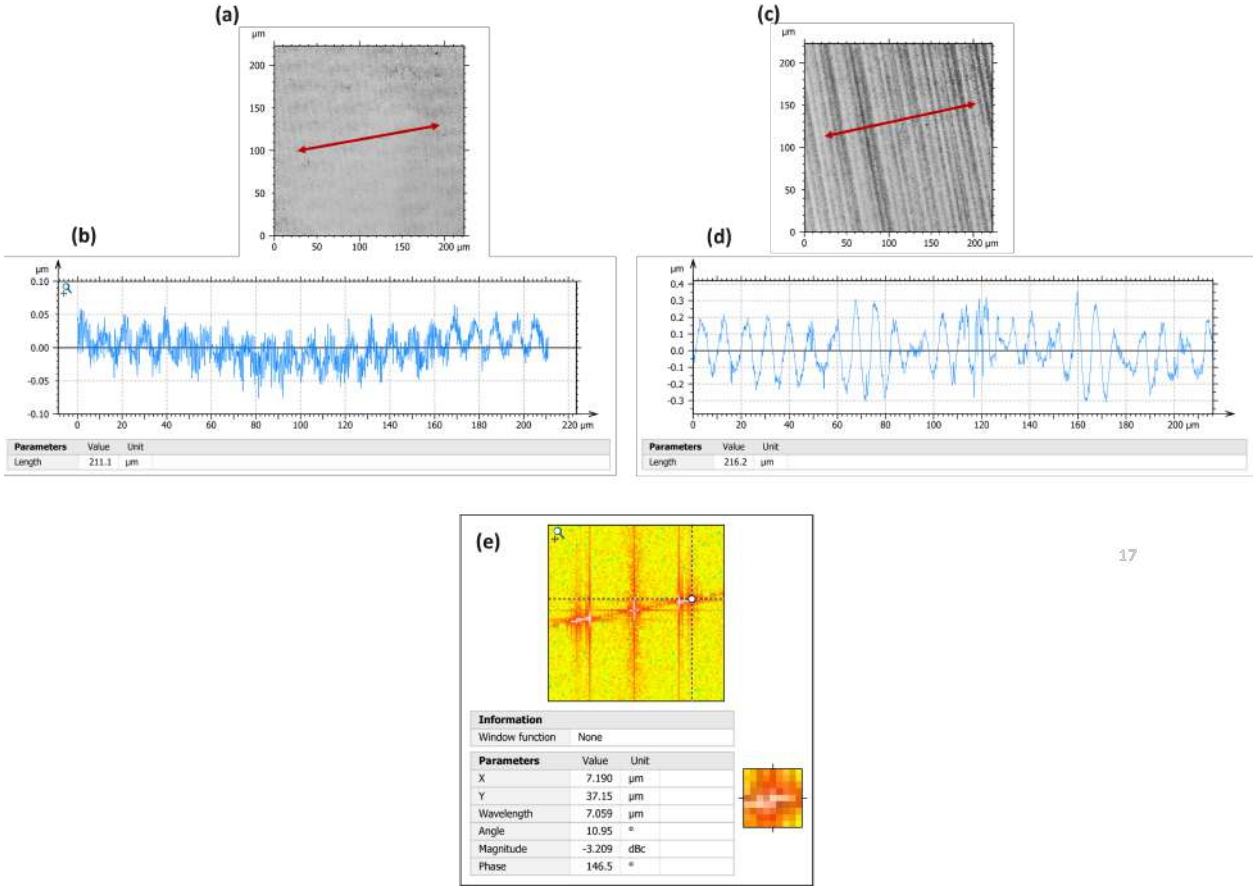

Figure 21 : The change in the structure with different overlaps at $h = 15\ \mu m$. **(a)** Microscope image of stainless steel at 50% overlap, **(b)** line profile corresponding to the red line in the structure in (a), **(c)** microscope image of stainless steel at 90% overlap, **(d)** line profile corresponding to the red line in the structure in (c), **(e)** fast Fourier transform of the structure in (c).

On the other hand, at $h = 22\ \mu m$ the structure was more homogeneous and the FFT contained a distinct periodicity, as can be observed from the line profile and the FFT in Fig. 22. In this case, the aspect ratio (AR), defined as the depth-to-period ratio, was 0.03.

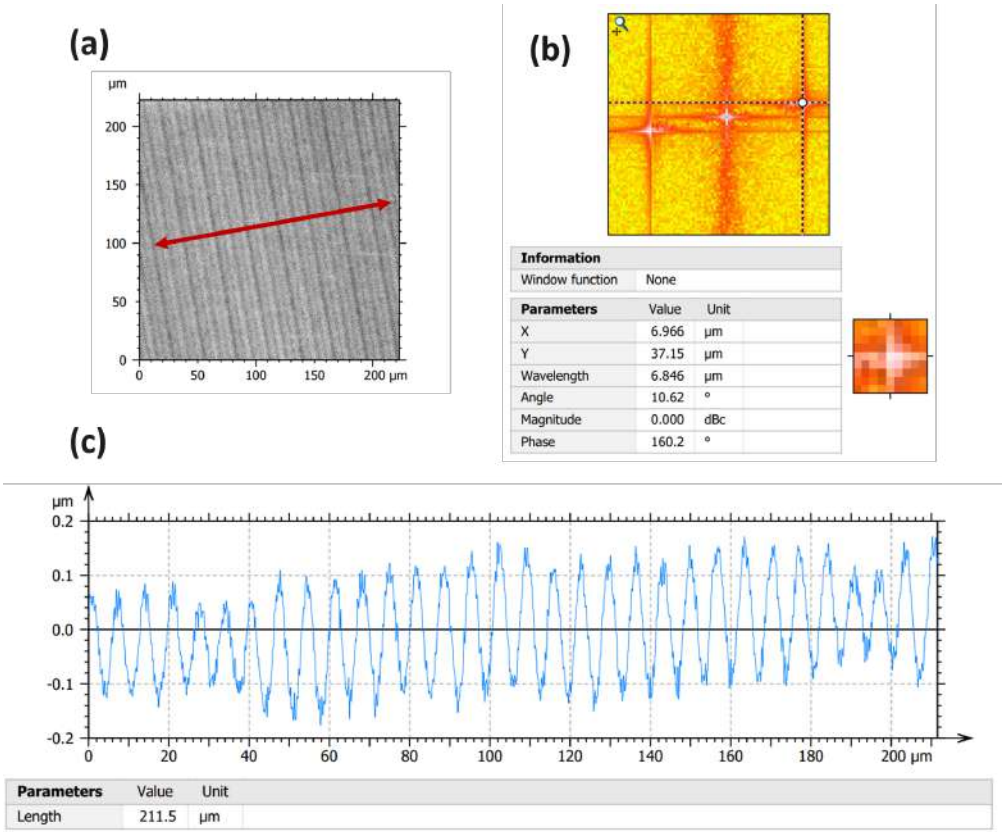

Figure 22 : **(a)** Microscope image of stainless steel at $h = 22\ \mu m$ and 80% overlap, **(b)** fast Fourier transform of the structure in (a).**(c)** The line profile corresponding to the red line in the structure in (a).

As the number of passes applied on the same pattern was increased, the fluence accumulated in the material, leading to deeper grooves in the sample and hence a higher AR. Figure 23 shows this effect and how the AR was increased from 0.03 to 0.08 at $h = 22\ \mu m$ and 80% overlap, by increasing the number of passes on the sample. It is expected that with further increases in the number of passes, the AR will reach a point of saturation.

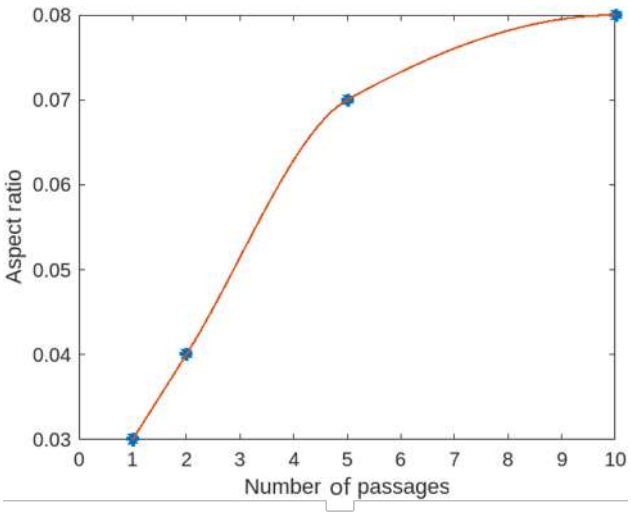

Figure 23 : Dependence of the aspect ratio on the number of passes. At $h = 22\ \mu m$ and 80% overlap, the number of passes was increased from 1 to 10.

From this initial investigation, certain optimal parameters were set to serve as a starting point for the study involving sapphire: The hatch value was selected as $h = 22\ \mu m$, and the maximum number of passages was set at 10. However, it is essential to recognize that these optimal parameters might require some adjustments when processing sapphire. As shown in Fig. 24, two matrices were engraved on sapphire at the same hatch $h = 22\ \mu m$ with different parameters. Each matrix corresponds to a different repetition rate: 175 kHz and 87 kHz. Each column corresponds to a different overlap (speed), and the rows correspond to a different number of passages.

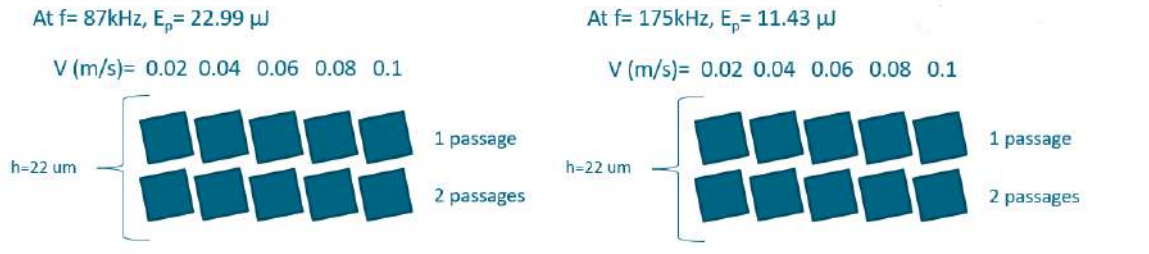

Overlap p in %	99.7	99.3	99	98.7	98.4
Speed (m/s)	**0.02**	**0.04**	**0.06**	**0.08**	**0.1**

Overlap p in %	99.8	99.7	99.5	99.3	99.2
Speed (m/s)	**0.02**	**0.04**	**0.06**	**0.08**	**0.1**

Figure 24 : Two matrices were engraved on sapphire at the same hatch $h = 22\ \mu m$ with different parameters. Each matrix corresponds to a different repetition rate: 87 kHz **(left)** and 175 kHz **(right)** and. Each column corresponds to a different overlap (speed), and the rows correspond to a different number of passages. The corresponding speeds for every overlap are shown in the table below each matrix.

At $f = 175kHz, v = 0.1m/s$ and for one pass, the line profile in Fig. 25b which corresponds to the red line in Fig. 25a shows the expected period of $\Lambda = 7.3\ \mu m$. However, the period from the

hatch $h = 22\ \mu m$ can also be observed from the superimposition of the interference maxima of the DLIP pulses, suggesting the need to adjust the hatch in future experiments.

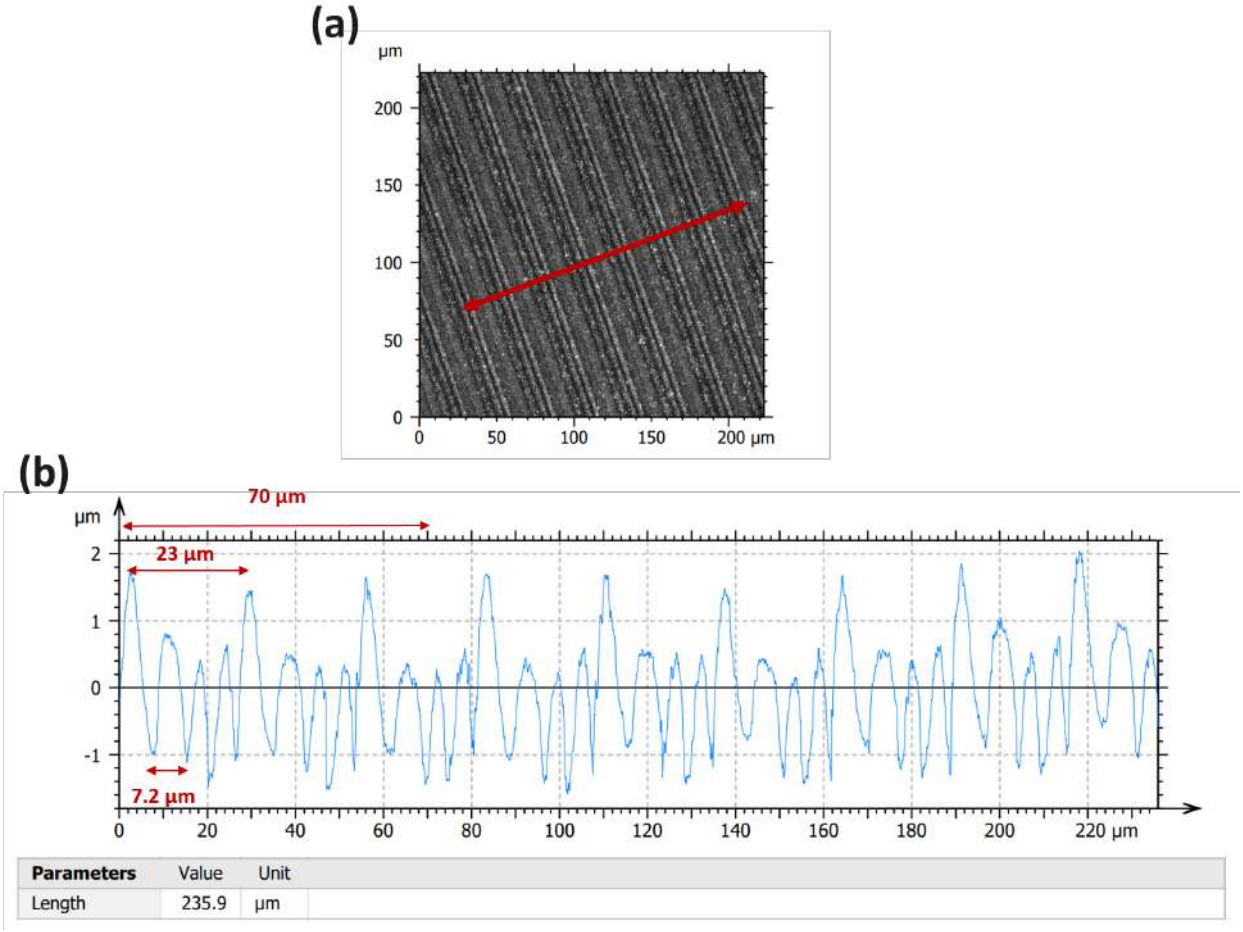

Figure 25 : **(a)** Microscope image of sapphire at $h = 22\ \mu m$, $v = 0.1 m/s$ and for one pass, **(b)** line profile corresponding to the red line in the structure in (a).

The period of the 1D fringe is given by: $\Lambda = \frac{\lambda}{2sin(\theta)}$, where $sin(\theta) = \frac{d}{F}$, and where d is the distance between the beams and F is the focal length of the used lens. Hence the periodicity can be lowered by using a short focal length.

For the same setup, the $F100mm$ lens was replaced by an $F30mm$ lens. As a result, the period was decreased from $\Lambda = 7.3\ \mu m$ to $\Lambda = 2.1\ \mu m$, as illustrated in the pattern obtained on stainless steel at a pulse energy of $5.21\ \mu J$ and an overlap of 90% in Fig. 26. LIPSS were also visible in the fringes, suggesting that the absorption mechanism is mainly dictated by multiphoton absorption.

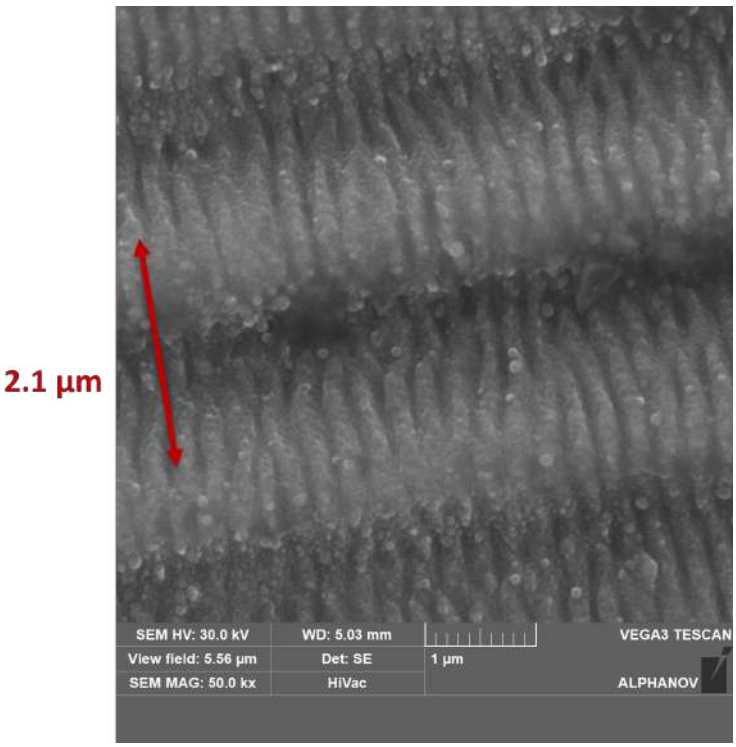

Figure 26 : SEM image of the obtained 2 beams interference pattern on stainless steel with an f-theta lens with a focal length of 30mm, at a pulse energy of 5.21 μJ and an overlap of 90%. The period is decreased to $\Lambda = 2.1\ \mu m$. LIPSS structures can also be observed

5.2 Four-beams DLIP

The four-beams configuration was applied first to a stainless steel sample. With a beam separation of 0.3 cm, the obtained periodicity was $\Lambda = 5.3\ \mu m$, as shown in Fig. 27.

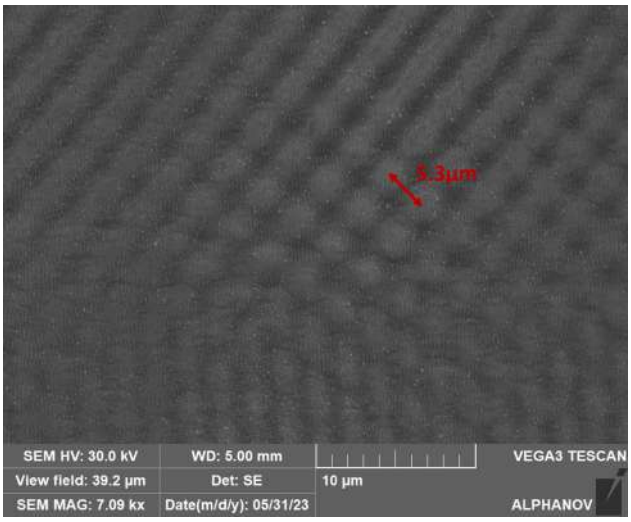

Figure 27 : SEM image of the four-beams configuration on a stainless steel sample at a pulse energy of 0.97 J and an overlap of 60%. With a beam separation of 0.3 cm, the obtained periodicity was $\Lambda = 5.3\ \mu m$.

To obtain a smaller period, the separation between the diffracted beams should be increased.

However, the diameter of the entrance of the scanner (Scanlab hurrySCAN II 14) restricted the separation that could be attained. Upon upgrading to a scanner with a larger entrance (Scanlab excilliSCAN 20), the separation between the beams was increased to 1.2 cm, leading to a periodicity of $\Lambda = 1.2\ \mu m$, as depicted in the patterns produced on PC in Fig. 28a and b.

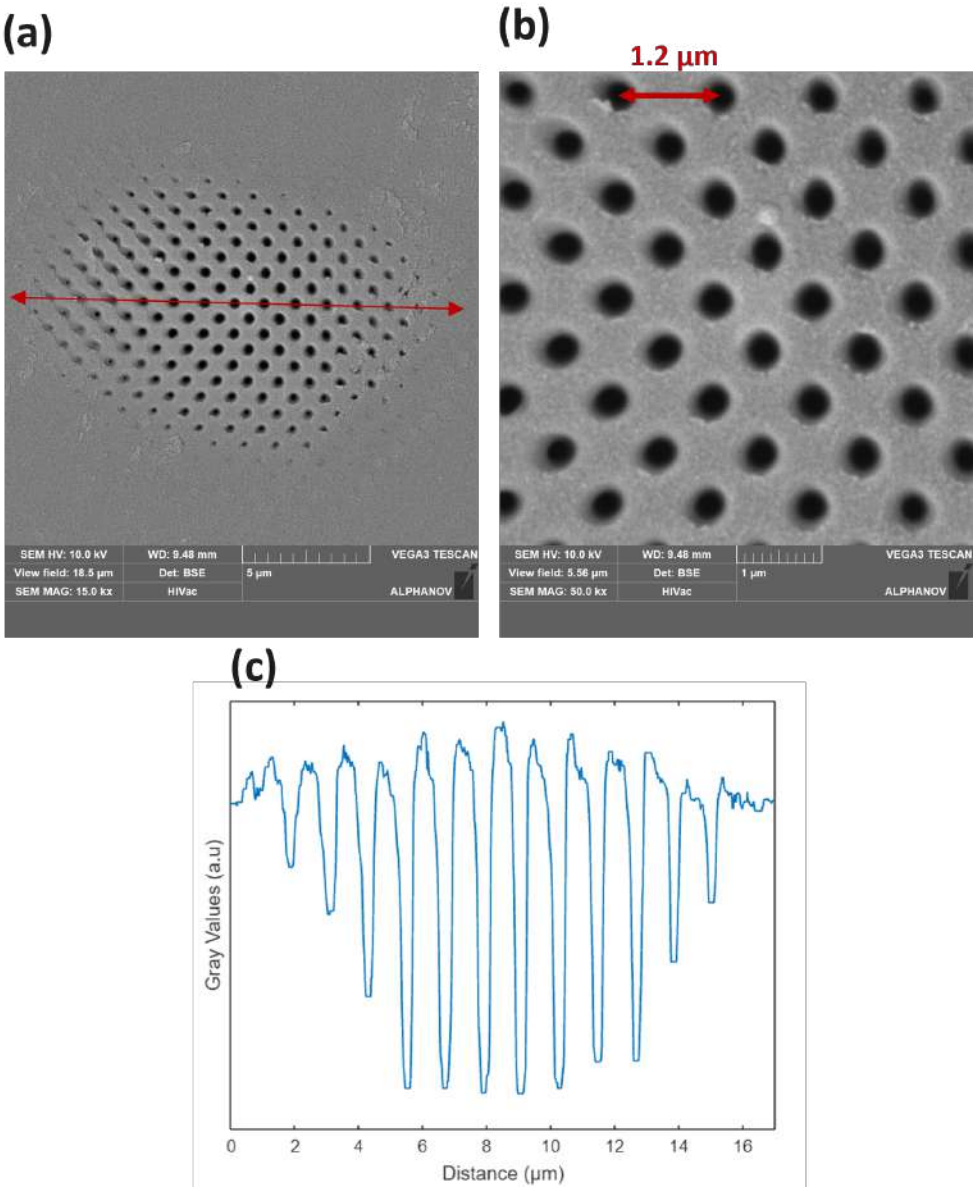

Figure 28 : SEM images showing periodic hexagonal structures produced on PC, at 15kx **(a)** and 50kx **(b)** magnification of the 4-beams configuration on the PC sample. With a beam separation of 1.2 cm, the obtained periodicity was $\Lambda = 1.2\ \mu m$. **(c)** The line profile corresponding to the red line in (a).

In this framework, a parametric study on PC was performed. As a preliminary step, the pulses were separated ($f = 100\ kHz, v = 2\ m/s$) to obtain the tilt angle $\alpha = 10°$, the spot diameter $d_i = 13.8\ \mu m$, and the periodicity $\Lambda = 1.2\ \mu m$. One pulse is depicted in Fig. 28a. The line profile in Fig.28c, which corresponds to the red line in Fig.28a, revealed the well-defined periodic patterns,

which perfectly match the periodic intensity distribution in Fig. 7c. The diameter value from Fig. 28a was used to compute the pulse separation distances corresponding to overlaps ranging from 50% to 90%. These computed values, along with their corresponding scanner speeds, are presented in Table 3. Unlike the case of the 1D fringes configuration, the hexagonal structure exhibits periodicity along the vertical direction as well, therefore, the distances were rounded to integer multiples of the period to avoid damaging the structures created in previous pulses.

Table 3 . The different pulse separation distances corresponding to different overlaps, and the corresponding scanner speed.

Overlap p in %	50	60	70	80	90
Distance between successive pulses (µm)	6.6	5.28	3.96	2.64	1.32
Rounding the distance to have an integer multiple of the period (µm)	6	4.6	3.6	2.4	1.2
Corresponding overlap (%)	55	64	73	82	91
Speed (m/s)	**0.6**	**0.48**	**0.36**	**0.24**	**0.12**

The overlaps were produced under varying pulse energies. Table 4 provides a summary of these overlaps, indicating their quality: red squares denote damaged structures, orange squares represent structures that are not damaged but lack homogeneity and green squares indicate surfaces with high overall homogeneity and quality. The ablation was observed first at a pulse energy of $E_p = 0.41\ \mu J$. When the overlap and the pulse energy were increased, the structures were damaged due to pulse accumulation, as exemplified by the structure created at the highest overlap (90%) and the highest pulse energy ($E_p = 1.00\ \mu J$) shown in Fig. 29. Consequently, the optimal overlap was selected to be within the range of 50% and 70% for pulse energies ranging from 0.51 μJ to 0.81 μJ.

Table 4 . The overlaps were produced under varying pulse energies. The red squares denote damaged structures, the orange squares represent structures that are not damaged but lack homogeneity and the green squares indicate surfaces with high overall homogeneity and quality.

Overlap / E_p	90%	80%	70%	60%	50%
0.41 μJ					
0.51 μJ					
0.60 μJ					
0.70 μJ					
0.81 μJ					
0.91 μJ					
1.00 μJ					

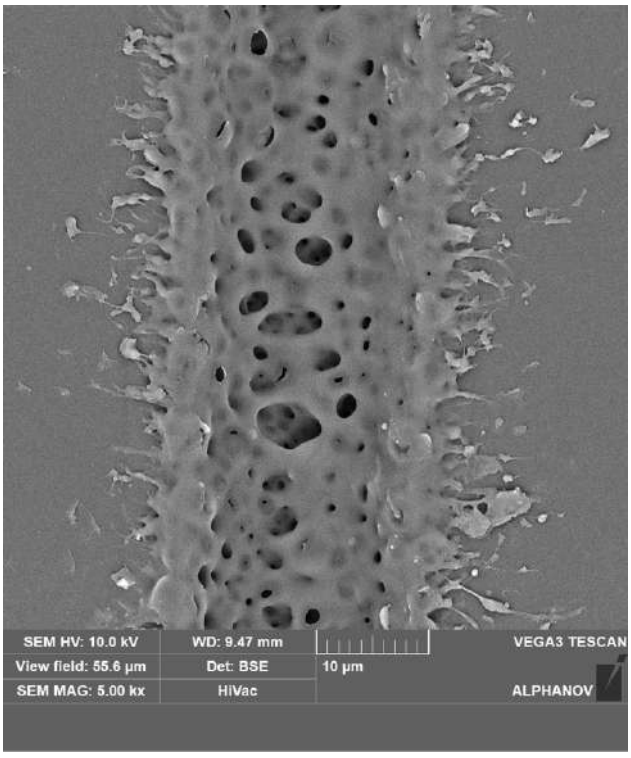

Figure 29 : SEM image of the line made at the highest overlap (90%) and the highest pulse energy E_p = 1.00 μJ, the accumulation of the fluence caused the material to be damaged.

An important observation is that as the overlap was increased to 70%, the periodicity decreased to 0.6 μm, as clearly indicated in the graph presented in Fig. 30. This can be explained by the positioning of the intensity maxima, which lands between the previously engraved holes, leading to half of the period obtained from looking at a single pulse, as depicted in Fig. 31b. Moreover, the

diameter of the holes at this overlap was 251 ± 86 *nm*, which is smaller than the visible wavelength range of the light, making them suitable to form a gradient refractive index layer, and hence allowing the incident light to gradually 'bend' into the substrate and reduce the reflection of the incident light. However, it is noteworthy that the lines produced at a 50% overlap exhibited superior homogeneity. Consequently, a single optimal combination of pulse energy and overlap (speed) was selected for further investigation of the hatch parameter: $E_p = 0.81\ \mu J$ with a 50% overlap. At these specified values, no significant thermal effects were observed, and the resulting hexagonal patterns were visible, as shown in Fig. 31c and d. Moreover, at this optimum condition, the diameter of the holes was 205 ± 49 *nm*, also showing the potential for anti-reflection applications by suppressing the reflection from wavelengths higher than the dimensions of the hole. Furthermore, a lower diameter of 147 ± 27 *nm* was achieved at a lower pulse energy of 0.5 μJ while maintaining the same degree of overlap (50%). The graph in Fig. 32 presents the diameters obtained at 50% overlap with varied pulse energies. When the pulse energy increases, a larger amount of the material is ablated at the areas corresponding to the interference maxima, leaving behind craters with a larger diameter.

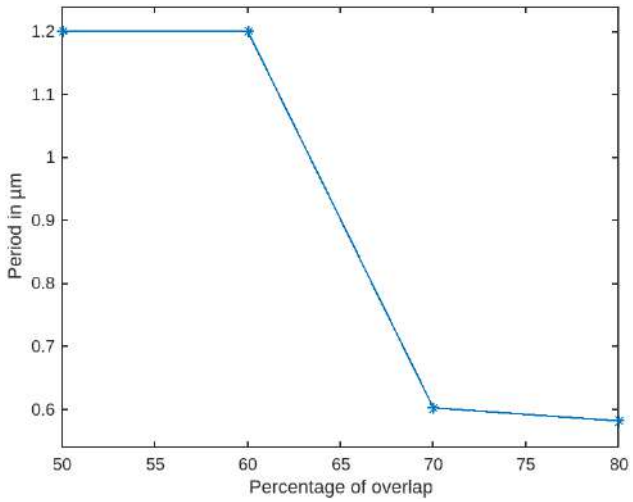

Figure 30 : The change in the spatial period of the obtained patterns as a function of the overlap at $E_p = 0.51\ \mu J$.

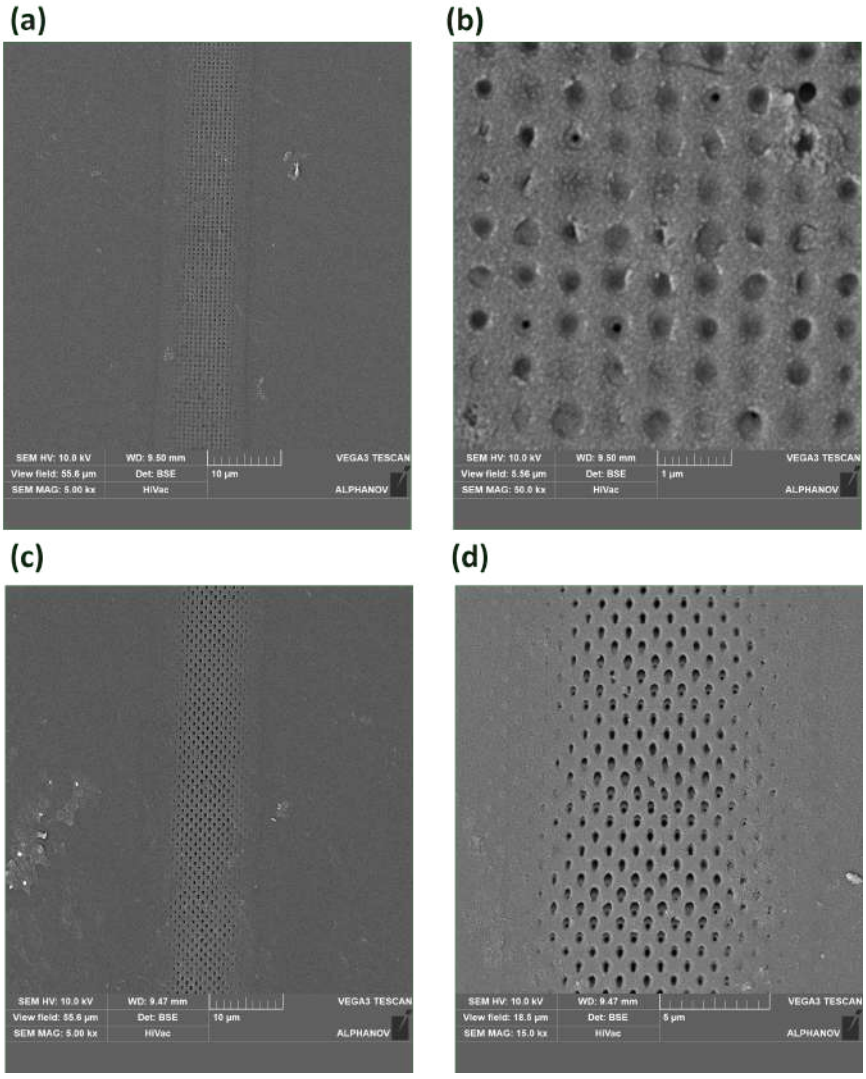

Figure 31 : The line resulting from $E_p = 0.6\ \mu J$ and an overlap of 70% at magnification 5.00kx **(a)** and 50kx **(b)**, and the line obtained at $E_p = 0.81\ \mu J$ and an overlap of 50% at magnification 5.00kx **(c)** and 15kx **(d)**.

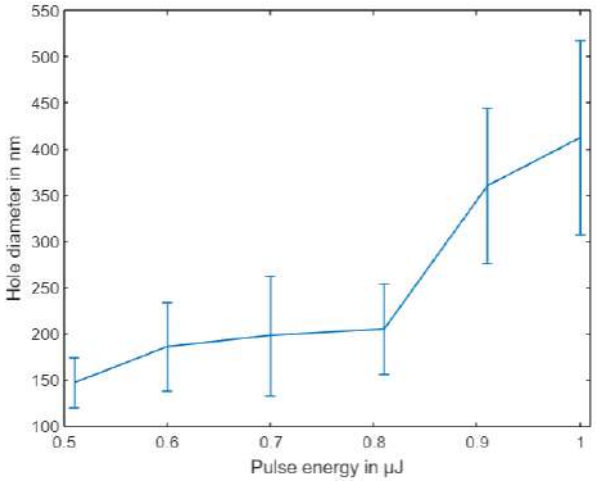

Figure 32 : Curve of the diameters of the holes obtained at 50% overlap with varied pulse energies from 0.5 μJ to 1 μJ.

Since the period was $\Lambda = 1.2\ \mu m$, the hatch was selected as an integer multiple of Λ: h= 6, 8, 12, 14 μm in order to pattern larger areas ($2x2mm^2$ squares). Figures 33a and 33b show that at hatches 6 and 8 μm, respectively, the patterns were destroyed and the material was damaged. When the lines were separated further by increasing the hatch to 12 μm and 14 μm, as depicted in figures 33c and 33d, the patterns could be observed. However, the overlap between the pulses was not uniform, as evidenced by the distinguished individual pulses, suggesting the need for selecting a different overlap value for future experiments. Additionally, within the same square, certain regions in the middle were ablated, while other parts along the edges were damaged. This observation suggests that the acceleration and deceleration in the movement of the mirrors inside the scanner are affecting the overlap between the pulses. This can be rectified by correcting the sky-writing mode or through the implementation of additional synchronization between the scanning mirror's position and the generation of laser pulses. Hence, further investigations are yet to be done in the future in order to optimize the process and obtain more homogeneous structures in larger areas, and to characterize the optical properties of the obtained structures.

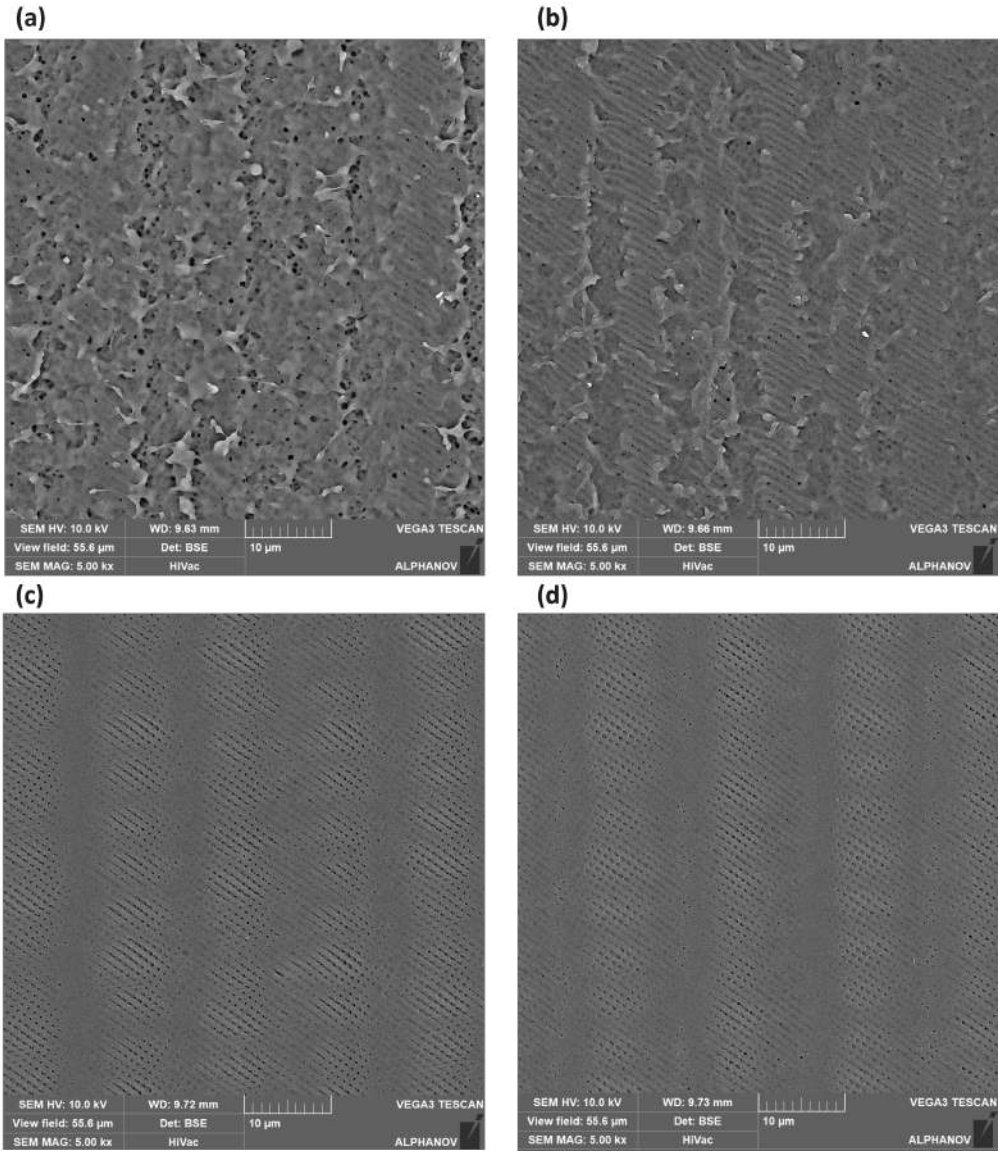

Figure 33 : $2x2mm^2$ squares at 50% overlap and hatches of 6 μm **(a)**, 8 μm **(b)**, 12 μm **(c)**, and 14 μm **(d)**.

6 Conclusions and outlook

1. The feasibility of producing micropatterns on sapphire and polycarbonate by non-linear absorption of interfering laser beams (two beams and four beams) was demonstrated.

2. It was also shown that using a lens with a large entrance pupil and a short focal length (F30mm) enabled the achievement of smaller periodicity. For the same setup, the periodicity was decreased from 7.3 μm to 2.3 μm.

3. With a higher aperture scanner, it was possible to separate the beams more and lower the periodicity from 5.3 μm to 1.2 μm. These structures produced on PC contained holes with a diameter down to 147 ± 27 nm, indicating the potential for mitigating reflection from wavelengths exceeding this diameter value, thereby highlighting its suitability for anti-reflection purposes.

4. Further investigations need to be done in order to optimize the process and study the modified surface properties.

References

[1] P. Gregorčič, M. Conradi, L. Hribar and M. Hočevar, Long-Term Influence of Laser-Processing Parameters on (Super)hydrophobicity Development and Stability of Stainless-Steel Surfaces, Materials **11**(11), 2240 (2018).

[2] E. Stratakis, J. Bonse, J. Heitz, J. Siegel, G. Tsibidis, E. Skoulas, A. Papadopoulos, A. Mimidis, A.-C. Joel, P. Comanns, J. Krüger, C. Florian, Y. Fuentes, J. Solis and W. Baumgartner, Laser engineering of biomimetic surfaces, Mater. Sci. Eng. R Rep. **141**, 100562 (2020).

[3] H. Ensikat, P. Ditsche, C. Neinhuis and W. Barthlott, Superhydrophobicity in perfection: The outstanding properties of the lotus leaf, Beilstein J. Nanotechnol. **2**, 152–61 (2011).

[4] E. Hein, D. Fox and H. Fouckhardt, Glass surface modification by lithography-free reactive ion etching in an Ar/CF4-plasma for controlled diffuse optical scattering, Surf. Coat. Technol. **205**, S419–S424 (2011).

[5] R. Garcia, A. Knoll and E. Riedo, Advanced scanning probe lithography, Nat. Nanotechnol. **9**, 577–87 (2014).

[6] M. P. Lim, X. Guo, E. L. Grunblatt, G. M. Clifton, A. N. Gonzalez and C. N. LaFratta, Augmenting mask-based lithography with direct laser writing to increase resolution and speed, Opt. Express **26**, 7085–7090 (2018).

[7] L. Mulko, M. Soldera and A. F. Lasagni, Structuring and functionalization of non-metallic materials using direct laser interference patterning: a review, Nanophotonics **11**(2), 203–240 (2022).

[8] M. Soldera, S. Alamri, P. Sürmann, T. Kunze and A. Lasagni, Microfabrication and Surface Functionalization of Soda Lime Glass through Direct Laser Interference Patterning, J. Nanomater. **11**, 129 (2021).

[9] D. Müller, T. Fox, P. Grützmacher, S. Suarez and F. Mücklich, Applying Ultrashort Pulsed Direct Laser Interference Patterning for Functional Surfaces, Sci. Rep. **10**, 3647 (2020).

[10] H. Butt, A. Yetisen, D. Mistry, S. Khan, U. Hassan and S. Yun, Morpho Butterflies: Morpho Butterfly-Inspired Nanostructures, Adv. Opt. Mater. **4**, 489–489 (2016).

[11] R. Siddique, G. Gomard and H. Hölscher, The role of random nanostructures for the omnidirectional anti-reflection properties of the glasswing butterfly, Nature communications **6**, 6909 (2015).

[12] S. Milles, M. Soldera, T. Kuntze and A. Lasagni, Characterization of self-cleaning properties on superhydrophobic aluminum surfaces fabricated by direct laser writing and direct laser interference patterning, Appl. Surf. Sci. **525**, 146518 (2020).

[13] D. Huerta-Murillo, A. Aguilar, S. Alamri, J. Cardoso, R. Jagdheesh, A. Lasagni and J. L. Ocaña, Fabrication of multi-scale periodic surface structures on Ti-6Al-4V by direct laser writing and direct laser interference patterning for modified wettability applications, Opt. Lasers Eng. **98**, 134–142 (2017).

[14] A. Madelung, S. Alamri, T. Steege, B. Krupop, A. Lasagni and T. Kunze, Scanner-Based Direct Laser Interference Patterning on Stainless Steel, Adv. Eng. Mater. **23**, 2001414 (2021).

[15] I. Gnilitskyi, T. J. Derrien, Y. Levy, N. Bulgakova, T. Mocek and L. Orazi, High-speed manufacturing of highly regular femtosecond laser-induced periodic surface structures: Physical origin of regularity, Sci. Rep. **7**, 8485 (2017).

[16] L. Gemini, G. Mincuzzi, M. Faucon and R. Kling, Surface Functionalization by Double Ultrashort Laser Pulses: A Review, J. Jpn. Laser Process. Society **29**, 11 (2022).

[17] G. Burrow and T. Gaylord, Multi-Beam Interference Advances and Applications: Nano-Electronics, Photonic Crystals, Metamaterials, Subwavelength Structures, Optical Trapping, and Biomedical Structures, Micromachines **2**, 221–257 (2011).

[18] K. Sugioka and Y. Cheng, *Ultrafast laser processing: From micro-to nanoscale*, Pan Stanford (2013).

[19] Z. Lin and M. Hong, Femtosecond Laser Precision Engineering: From Micron, Submicron, to Nanoscale, Ultrafast Sci. **2021**, 1–22 (2021).

[20] R. Gattass and E. Mazur, Femtosecond Laser Micromachining in Transparent Materials, Nat. Photonics **2**, 219–225 (2008).

[21] S. Mao, F. Quere, S. Guizard, X. Mao, R. Russo, G. Petite and P. Martin, Dynamics of Femtosecond Laser Interactions with Dielectrics, Appl. Phys. A **79**, 1695–1709 (2004).

[22] F. He, Y. Liao, J. Lin, J. Song, L. Qiao, Y. Cheng and K. Sugioka, Femtosecond Laser Fabrication of Monolithically Integrated Microfluidic Sensors in Glass, J. Sens. **14**, 19402–19440 (2014).

[23] W. J. Reichman, *Understanding How Femtosecond Laser Waveguide Fabrication in Glasses Works*, Ph.D. thesis (2006).

[24] S. J. Mihailov, *Femtosecond Laser-Inscribed Fiber Bragg Gratings for Sensing Applications*, Heinemann (2018).

[25] L. V. Keldysh, Ionization in the Field of a Strong Electromagnetic Wave, Sov. Phys. JETP **20**, 1307 (1965).

[26] A. Peter, A. Lutey, S. Faas, L. Romoli, V. Onuseit and T. Graf, Direct laser interference patterning of stainless steel by ultrashort pulses for antibacterial surfaces, Opt. Laser Technol. **123**, 105954 (2019).

[27] S. Milles, V. Vercillo, S. Alamri, A. Aguilar, T. Kunze, E. Bonaccurso and A. Lasagni, Icephobic Performance of Multi-Scale Laser-Textured Aluminum Surfaces for Aeronautic Applications, J. Nanomater. **11**, 1–17 (2021).

[28] Y. Park, J. Berger, Z. Tang, L. Müller-Meskamp, A. Lasagni, K. Vandewal and K. Leo, Flexible, light trapping substrates for organic photovoltaics, Appl. Phys. Lett. **109**, 093301 (2016).

[29] S. Alamri, A. Aguilar and A. Lasagni, Controlling the Wettability of Polycarbonate substrates by producing hierarchical structures using Direct Laser Interference Patterning, Eur. Polym. J. **99**, 27–37 (2017).

[30] B. Voisiat, S. Indrisiunas, R. Suzanovièiene, I. Šimkiene and G. Raciukaitis, Formation of Periodic Structures on Silicon by Laser Beam Interference Ablation Technique for Light Control in Solar Cells, Proc. SPIE - Int. Soc. Opt. **9180**, 918009 (2014).

[31] K. Kawamura, N. Sarukura, M. Hirano and H. Hosono, Holographic Encoding of Permanent Gratings Embedded in Diamond by Two Beam Interference of a Single Femtosecond Near-Infrared Laser Pulse, Jpn. J. Appl. Phys. **39**, L767–L769 (2000).

[32] K. Kawamura, N. Sarukura, M. Hirano, N. Ito and H. Hosono, Periodic nanostructure array in crossed holographic gratings on silica glass by two interfered infrared-femtosecond laser pulses, Appl. Phys. Lett. **79**, 1228–1230 (2001).

[33] Y. Han and S. Qu, Controllable fabrication of periodic hexagon lattice on glass by interference of three replicas split from single femtosecond laser pulse, Laser Phys. **19**, 1067–1071 (2009).

[34] K. Kawamura, T. Ogawa, N. Sarukura, M. Hirano and H. Hosono, Fabrication of surface relief gratings on transparent dielectric materials by two-beam holographic method using infrared femtosecond laser pulses, Appl. Phys. B **71**, 119–121 (2000).

SURFACE FUNCTIONALIZATION OF TRANSPARENT MATERIALS BY DIRECT LASER INTERFERENCE PATTERNING

Kawthar Reggui

Summary

Transparent materials find widespread use in well-established and emerging industries, including microelectronics, photovoltaics, optical components, and biomedical devices. Consequently, the surface functionalization of these materials represents a promising approach to customizing their properties for applications in these fields. Direct Laser Interference Patterning (DLIP) stands out as a versatile method for creating precisely defined microstructures. DLIP involves the superposition of multiple laser beams to generate an interference pattern on the surface of the material. Through precise manipulation of several parameters such as the number of interfering beams, their angle of overlap, the wavelength of the laser radiation, and the applied fluence, a diverse range of patterns, periodicities, and aspect ratios can be attained.

For anti-reflection applications in the visible range, the structures have to reach values that are much smaller than the sub-micron scale (< 300 nm). Since the spatial period of the obtained patterns depends on the beam wavelength and overlapping angle θ, it is necessary to work at short wavelengths (e.g. UV) and increase the overlapping angle to obtain very small structures. Hence, in this work, DLIP was performed on two transparent materials, sapphire, and polycarbonate (PC), using a custom-made f-theta lens with a large aperture (d=20 mm) and a small focal length (F30mm), with the 3rd harmonic (343 nm) of femtosecond ytterbium laser.

The feasibility of producing micropatterns on sapphire and PC by non-linear absorption of interfering laser beams (two beams and four beams) was demonstrated. It was also shown that using a lens with a large entrance pupil and a short focal length enabled decreasing the periodicity from 7.3 μm to 2.3 μm for the same setup. Moreover, with a higher aperture scanner, it was possible to separate the beams as much as possible and hence lower the periodicity from 5.3 μm to 1.2 μm. These structures contained holes with a diameter down to 147 ± 27 nm, making them suitable for anti-reflection purposes. The impact of the pulse energy, the number of passages, and the overlap of pulses on the structure were also investigated. Yet, further investigations need to be done to optimize the process and study the optical properties of the modified surfaces.